#### **Research Article**

Nuralhuda Aladdin Jasim\*, Shahlaa Esmail Ebrahim, and Saad H. Ammar

# Visible light-boosted photodegradation activity of Ag-AgVO<sub>3</sub>/Zn<sub>0.5</sub>Mn<sub>0.5</sub>Fe<sub>2</sub>O<sub>4</sub> supported heterojunctions for effective degradation of organic contaminates

https://doi.org/10.1515/eng-2022-0585 received October 10, 2023; accepted January 03, 2024

**Abstract:** One of the most important concerns in developing efficient heterojunction photocatalysts for the photodegradation of environmental contaminants is the enhancement and acceleration of photocarrier separation. In this study, novel nanocomposite photocatalysts of Ag-AgVO<sub>3</sub> nanorods grafted with Zn<sub>0.5</sub>Mn<sub>0.5</sub>Fe<sub>2</sub>O<sub>4</sub> metal ferrites nanoparticles were developed by using facial hydrothermal and coprecipitation techniques for the effective photodegradation of Rhodamine B (Rh B) under visible light exposure. The fabricated materials were analyzed in detail using scanning electron microscopy, energy-dispersive X-ray spectroscopy (EDS), nitrogen adsorption/desorption, transmission electron microscopy (TEM), photoluminescence spectroscopy (PL), vibrating sample magnetometer, and ultraviolet-visible diffuse reflectance spectroscopy (DRS). The results showed an efficient contribution when compared to the earlier research. The TEM showed a hybrid of nanorods of supported composite with metal ferrite and Ag attached on the surface, consistent with field emission scanning electron microscopy and EDS results. The DRS expressed a lower band gap for supported nanocomposites (1.5 eV), which, arranged with PL, showed a lower recombination rate of supported nanocomposites. The surface properties showed that the supported hybrid might be as small as 45.42 nm or as large as 20.33 nm compared with others. When comparing the photocatalytic activity of pure AgVO<sub>3</sub>, Ag/AgVO<sub>3</sub>, and Zn<sub>0.5</sub>Mn<sub>0.5</sub>Fe<sub>2</sub>O<sub>4</sub> photocatalysts, the performance of Ag-AgVO<sub>3</sub>/Zn<sub>0.5</sub>Mn<sub>0.5</sub>Fe<sub>2</sub>O<sub>4</sub> nanocomposite photocatalyst was clearly superior (more than 99.9% degradation efficiency was achieved). The boosted activity the Ag-AgVO<sub>3</sub>/Zn<sub>0.5</sub>Mn<sub>0.5</sub>Fe<sub>2</sub>O<sub>4</sub> photocatalyst system was justified by Z-system heterojunction induced by the plasmonic effect, and the suggested mechanism was investigated by quenching of reactive species by scavengers. The degradation performance was achieved under optimum conditions (pH = 2, 20ppm of pollutant concentration, 120 mM of hydrogen peroxide, 1 g/L of catalysts dose). The results showed that after 240 min of visible irradiation resulted in the high (chemical oxygen demand) and (total organic carbon) reductions with a removal efficiency of (85) to (90%) for Rh B dye. The fabricated Ag-AgVO<sub>3</sub>/Zn<sub>0.5</sub>Mn<sub>0.5</sub>Fe<sub>2</sub>O<sub>4</sub> nanocomposites were effective in the degradation of organic pollutants in wastewater treatment.

**Keywords:** organic dyes, photocatalytic degradation, Ag–AgVO<sub>3</sub>/  $Zn_{0.5}Mn_{0.5}Fe_2O_4$ , supported heterostructure, visible-light responsive

#### 1 Introduction

A variety of industrial strategies currently exist to eliminate dyes-contaminated wastewater [1]. Photocatalysis is one of the preferred of these methods since it is fast, ecofriendly, effective, and cheap [2]. Using the energy obtained from solar illumination, pollutants in the wastewater can be entirely decomposed in a process that requires no further energy [3,4]. The photocatalysis process is used for a variety of environmental applications, including microbial inhibition, cancer cell eradication, and air pollution control [5]. This is accomplished by the production of free electrons and holes, in addition to reactive oxygen species (ROS) [6], such

**Shahlaa Esmail Ebrahim:** Environmental Engineering Department, College of Engineering, University of Baghdad, Baghdad, Iraq, e-mail: shahlaa.ebrahim@coeng.uobaghdad.edu.iq

Saad H. Ammar: Department of Chemical Engineering, College of Engineering, Al-Nahrain University, Jadriya, Baghdad, Iraq; College of Engineering, University of Warith Al-Anbiyaa, Karbala, Iraq, e-mail: saad.h.ammar@nahrainuniv.edu.iq

<sup>\*</sup> Corresponding author: Nuralhuda Aladdin Jasim, Environmental Engineering Department, College of Engineering, University of Baghdad, Baghdad, Wasit, Iraq; Department of Civil Engineering, Wasit University, Wasit, Iraq, e-mail: njasim@uowasit.edu.iq

as hydroxyl and superoxide radicals and hydrogen peroxide (H<sub>2</sub>O<sub>2</sub>), which combines with organic contaminants to generate anoxic intermediates [7].

Different fabrication methods are utilized to synthesize nanoparticles [8]. Yao et al. [9] stated that the fabrication of nanoscale non-smooth fibers with high geometric potential and the non-linear vibration of nanoparticles. The relatively rough surface of a fiber on the nano- or micro-scale has an enormous surface area and an extraordinarily high surface energy, also known as geometric potential. The process of electrospinning a rough surface was deconstructed by regulating solvent evaporation and nanoscale attachment of nanoparticles to the surface. This work is designed to shed light on the fabrication of nanoscale porous nanofibers and lotus-surface-like nanofibers using poly (vinylidene fluoride), multi-walled carbon nanotubes, and a binary solvent solution [10]. Another important topic covered is the vibration of a nanoparticle close to its equilibrium, which has a significant impact on its surface morphology.

Tian et al. [11] outlined alternative techniques for creating "non-smooth fibers" using bubble electrospinning, fiber morphology, and the theoretical concepts and potential of geometrical design for the superhydrophilic or super-hydrophobic properties of nanofiber membranes. Within this concept, the nanoscale porous structure is the sole entity capable of displaying either attraction or repulsion. There is no way for a particle to be absorbed onto the surface of a smooth fiber because the reaction will be so intense that it will resist the particle. The hydrophilic or hydrophobic characteristics of a particle (such as a water molecule) are only revealed when it approaches the critical point of absorption or repulsion. By utilizing nanofibers, it is possible to fabricate gas-absorbing or -repelling membranes; for instance, one may construct an oxygen-enriched membrane or one that selectively absorbs CO<sub>2</sub> rather than N<sub>2</sub>.

Khadayeir et al. [12] state that the purpose of synthesizing an  $\alpha\text{-Fe}_2O_3$  thin layer on a glass basis was to test the samples' antibacterial and self-cleaning characteristics after adding cold plasma. The samples were manufactured using the chemical spray pyrolysis process, which is executed at a temperature of 450°C. The morphological and structural characteristics of  $\alpha\text{-Fe}_2O_3$  thin layers were examined using various imaging techniques both before and after plasma injection. Findings: the wettability and antibacterial characteristics of a hematite thin film with gram-negative and gram-positive bacteria were examined both before and after plasma injection, as this method shows great potential for altering the surface of thin films. The findings demonstrate that a small layer of  $\alpha\text{-Fe}_2O_3$  exposes plasma to notable morphological, self-cleaning, and antibacterial alterations.

Balasubramanian *et al.* [13] stated that one potential alternative is hydrogen, which involves using hydrogen-derived low-carbon fuels and fuel cell automobiles to decarbonize transportation, shipping, and aerial transportation. Semiconductors are used in a variety of industries, including aerospace, fertilizer, pharmaceutical, metal treatment, methanol, commercial nitrogen fixation from air reduction, power plant generator, and petroleum refining. Unsaturated lipids are transformed into saturated and greasy fats by hydrogen. Nuclear spins in hydrogen can be either *para-* or *ortho-*hydrogen. Hydrogen molecules consist of 75% *ortho-*hydrogen and 25% parahydrogen when they are at normal temperature. In order to advance in the field of hydrogen technology, it is essential to possess a comprehensive understanding of thermophysics.

Different types of catalysts are utilized in the treatment of advanced oxidation process (AOPs). AOPs are based on physicochemical reactions that alter molecular structures of chemical species in substantial ways [14]. Different approaches were used to remove organic pollutants including physicochemical techniques such as photolysis, photo-Fenton oxidation, electrooxidation, heterogeneous catalysis, and ozonation [15]. AOPs were thought to have optimal operating costs, zero secondary emissions, and better oxidation efficiency than traditional chemical processes. Jasim *et al.* [3] stated that using synthesized nanocomposites is efficient in removing organic pollutants such as dyes from industrial wastewater.

Metal ferrites have demonstrated outstanding features and efficiency across a wide range of commercial applications. Chemical stability, crystallinity, availability, minimal toxicity, and improved assets of narrow bandgap make them a perfect and highly effective photocatalyst [5]. The use of ferrite photocatalysts in the photocatalytic removal of organic pollutants has been the subject of many investigations [16]. Chen et al. [17] employed a reduction-oxidation technique to produce ZnFe<sub>2</sub>O<sub>4</sub>, which they then used to show that orange II dye could be decolored in a visiblelight-catalyzed shydrogen peroxide system [18]. Different synthesis of metal ferrites was used by Shakil et al. [19], who studied the deterioration of methylene blue dye in a light-irradiated acidic pH system [20]. Visible-light-assisted photocatalysis on morphologically different NiFe<sub>2</sub>O<sub>4</sub> photocatalysts generated by the hydrothermal process was shown in a previous study to be efficient in the removal of organic dyes. Even though this research discovered promising visible-light-driven photocatalysts for the breakdown of organic dyes, these photocatalysts suffered from major limitations such as slow degradation rates and high energy requirements. The objective is to synthesize metal ferrites as photocatalysts to decolorize under visible light with

minimum energy expenditure has been [21], in an effort to overcome these obstacles.

Due to the rapid photocarrier recombination, the photocatalytic process efficiency is highly constrained [22]. One of the approaches employed for reducing this drawback is heterogeneous junctions with other semiconductors to provide an easy path for charges and thus reduce recombination [23]. One example of a high photocatalytic activity semiconductor that can be doped with metal ferrites is Ag-based semiconductors, which possess outstanding possessions and have been extremely established as promising photocatalysts for photodegrading organic pollutants [24]. Particularly, silver vanadates have been extensively adopted due to their narrow bandgap, easy preparation, and good crystallization [25,26].

Jasim et al. [1] stated that dye usage has increased in Irag's thriving textile industry. Synthetic dyes continue to be widely employed due to their multiple benefits. A photocatalyst for the degradation of the synthetic dye Rhodamine B (Rh B) was synthesized using simple coprecipitation as a multimetal ferrite (Zn<sub>x</sub>Mn<sub>1-x</sub>Fe<sub>2</sub>O<sub>4</sub>). The effectiveness of photodegradation was evaluated by adjusting several reaction parameters, including acidity, catalyst dose, H<sub>2</sub>O<sub>2</sub> addition, dye concentration, and irradiation duration. Zn<sub>0.7</sub>Mn<sub>0.3</sub>Fe<sub>2</sub>O<sub>4</sub> shows an efficient degradation efficacy in removing organic pollutant. A mixture of 1 g/L catalyst, 20 mg/L Rh B, and 120 mM hydrogen peroxide expressed excellent degradation 99% degradation after 180 min of radiation irradiation. Rh B's degrading efficacy for total organic carbon (TOC) elimination and chemical oxygen demand (COD) reduction was 75 and 80%, respectively, at 20 ppm of Rh B.

Jasim et al. [3] reported that iron spinel ferrites with cobalt substitution ( $Co_x Zn_{1-x} Fe_2 O_4$ , x = 0 to 1) were formed. The porous material composed of aggregated ferrite nanoparticles, Co<sub>0.5</sub>Zn<sub>0.5</sub>Fe<sub>2</sub>O<sub>4</sub>, has pore widths ranging from 3 to 50 nm, with a minor peak at approximately 35 nm. Using Brunauer-Emmett-Teller (BET) computations, the surface area of  $Co_x Zn_{1-x} Fe_2 O_4$  was found to be 10.9 m<sup>2</sup>/g. The sample of  $Co_{0.3}Zn_{0.7}Fe_2O_4$  (x = 0.3) was proven to be 99% effective in removing the Rh B dye after 180 min of exposure to visible light. It was determined that the presence of OH and holes was the main reactive radicals that contributed to the degradation process using scavenger tests and fluorescence spectroscopy. An impressively stable photocatalyst composed of cobalt-zinc metal ferrites maintained its performance even after five consecutive cycles. In an ideal setting (pH = 2, catalyst dose = 0.1 mg, pollutant concentration = 20 mg/L, with 120 mM of hydrogen peroxide), the cobalt-zinc metal ferrites photocatalysts were determined to be the most effective in treating Rh B contaminated wastewater.

Jasim et al. [27] utilized the heterojunction photocatalysts for the photodegradation of environmental pollutants, which requires improved photocarrier separation. The most effective photocatalyst that degraded Rh B was Zn<sub>0.5</sub>Mn<sub>0.5</sub>Fe<sub>2</sub>O<sub>4</sub>@Ag-AgVO<sub>3</sub>, while Zn<sub>0.5</sub>Mn<sub>0.5</sub>Fe<sub>2</sub>O<sub>4</sub> and Ag-AgVO3 were also used in the experiment. After 180 min of exposure to 20 ppm Rh B, Zn<sub>0.5</sub>Mn<sub>0.5</sub>Fe<sub>2</sub>O<sub>4</sub>@Ag-AgVO<sub>3</sub> degraded 93.43%, leading to a maximum reduction of 90% in total organic carbon (TOC). After 120 min of visible light irridiation, the log (CFU) decreases of P. aeruginosa is attained to be 0.00001, demonstrating that nanocomposites are effective in bacterial inactivation. The Zn<sub>0.5</sub>Mn<sub>0.5</sub>Fe<sub>2</sub>O<sub>4</sub>@Ag-AgVO<sub>3</sub> photocatalyst helped remove organic contaminants and dangerous microorganisms from wastewater in a steady and effective manner.

Recent studies have indicated that semiconductors utilizing Ag as their basis material exhibit a narrow band gap energy, enabling them to exhibit significant absorption of visible light and demonstrate noticeable catalytic activity when exposed to visible light [28,29]. Nevertheless, the present study documented the utilization of silver vanadate (AgVO<sub>3</sub>) and Ag/AgVO<sub>3</sub>, as stated in the aforementioned research work.

Photocatalysts, produced and utilized in scientific research, are becoming more efficient in purifying polluted environments [30]. Therefore, in order to enhance the photocatalytic efficiency of supported Ag-AgVO<sub>3</sub>/Zn<sub>0.5</sub>Mn<sub>0.5</sub>Fe<sub>2</sub>O<sub>4</sub>, the present study investigated a novel methodology. In the first phase, Zn<sub>0.5</sub>Mn<sub>0.5</sub>Fe<sub>2</sub>O<sub>4</sub> and AgVO<sub>3</sub> were synthesized separately. The coprecipitation approach was used to directly produce composites of AgVO<sub>3</sub> and Zn<sub>0.5</sub>Mn<sub>0.5</sub>Fe<sub>2</sub>O<sub>4</sub>. Various methodologies were utilized to analyze the generated materials and composites. To assess the photocatalytic efficacy of each material and composite, they are subjected to testing using (Rh B) dyes. The research primarily focused on the kinetic modeling of dye degradation. The evaluation of photocatalytic dye degradation is conducted by quantifying the impact of electron scavengers. Various characteristics were thoroughly analyzed to verify that the nanocomposites exhibited superior degradation. An organic pollutant (Rh B) was utilized to study the photocatalytic activity of the nanocomposites when exposed to visible light irradiation (VLI).

Moreover, this work provides a comprehensive description of the construction and description of heterostructures synthesized from Zn<sub>0.5</sub>Mn<sub>0.5</sub>Fe<sub>2</sub>O<sub>4</sub>, AgVO<sub>3</sub>, and Ag–AgVO<sub>3</sub>/ Zn<sub>0.5</sub>Mn<sub>0.5</sub>Fe<sub>2</sub>O<sub>4</sub> for the purpose of photodegrading Rh B dye from the aqueous phase.

#### 2 Materials and methods

The study was designed to synthesize various nanocomposites such as Zn<sub>0.5</sub>Mn<sub>0.5</sub>Fe<sub>2</sub>O<sub>4</sub>, AgVO<sub>3</sub>, and supported nanocomposites Ag–AgVO $_3$ /Zn $_{0.5}$ Mn $_{0.5}$ Fe $_2$ O $_4$  and investigate the degradation performance using a batch reactor. The study was carried out in the Environmental Department at the University of Baghdad, College of Engineering. The data were analyzed using the SPSS program for the results regarding degradation efficiency, while the results of characterizations were performed using the Origin lab program.

#### 2.1 Materials

Different compounds were utilized in order to synthesize the supported nanocomposites.

Table 1 shows the materials utilized in the current research.

# 2.2 Synthesis of metal ferrites $Zn_{0.5}Mn_{0.5}Fe_2O_4$

Coprecipitation is used to create zinc-manganese ferrites  $(Zn_{0.5}Mn_{0.5}Fe_2O_4)$ . The iron nitrate concentration was 9.67 g per 100 mL of distilled water. Zinc nitrate, dissolved in around 0.9 M of distilled water, was used to synthesize zinc-manganese metal ferrite. Then, 100 mL of distilled water was mixed with manganese nitrate at different molar ratios. Different solutions were mixed in order to get the final solution, which has two various molarities

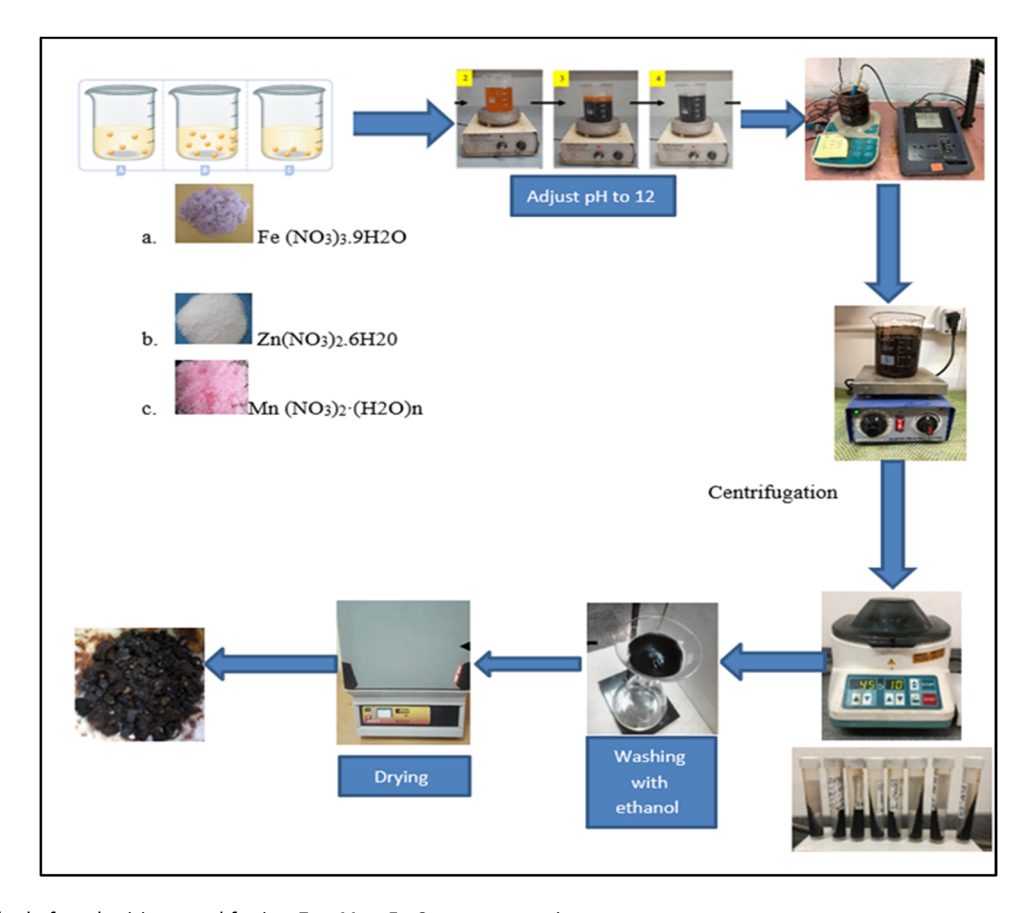
(0.5 M for both manganese and zinc salts and 0.4 M for iron-nitrate salts). A magnetic stirrer is used to thoroughly combine the solution after it has been made, a procedure that takes around 40 min. The solution is heated for around 30 min at 80°C. By gradually adding 3 M NaOH solution, the pH of the solution was raised to 11.9. The completed solution, which amounted to about 400 mL, was then transferred to plastic tubes in advance of being placed in a centrifuge. The final solution was washed three times with ethanol and distilled water and then dried at a specific degree of around (80–100)°C. The procedure is illustrated in Figure 1.

#### 2.3 Synthesis of AgVO<sub>3</sub> and Ag-AgVO<sub>3</sub>

The samples of silver vanadate were prepared using a straightforward hydrothermal method. The  $AgVO_3$  nanoribbons were synthesized by mixing 1:1 molar ratio (0.050 mol/L) solutions of  $AgNO_3$  and  $NH_4VO_3$  in two 25 mL volumes for 20 min. The newly formed suspension was then agitated for 3 h. The mixture was subjected to a temperature of  $180^{\circ}$ C for 24 h using a Teflon-lined stainless-steel autoclave hydrothermal reactor with a capacity of  $100 \text{ m}^3$ . After that, it was decided to allow the reactor to gradually cool to normal temperature. A pure  $AgVO_3$  sample was obtained using filtration, washing with 100% ethanol and distilled water, and vacuum drying at  $80^{\circ}$ C. The same procedure was used to synthesize the  $Ag/AgVO_3$  sample, with the exception that the molar ratio of  $AgNO_3:NH_4VO_3$  was 1.1:1 rather than 1:1.

Table 1: Chemical substances used in this current work

Chemicals	Chemical name	Purities (%)	Manufacturer	
Zinc nitrate	Zn(NO <sub>3</sub> ) <sub>2</sub> ·6H <sub>2</sub> O	99.9	HiMedia	
Manganese nitrate	$Mn(NO_3)_2 \cdot XH_2O$	99.9	Thoms Baker	
Iron nitrate	Fe(NO <sub>3</sub> ) <sub>3</sub> ·9H <sub>2</sub> O	99.9	Thomas Baker	
Sodium hydroxide	NaOH	99.88	SDFCL	
Ethanol	C <sub>2</sub> H <sub>5</sub> OH	100	Thomas Baker	
Sodium hydroxide	NaOH	99.88	BDH Limited Pool, England	
Silver nitrate	AgNO₃	99.8	Odaejung, China	
Ethanol	C <sub>2</sub> H <sub>5</sub> OH	100	Solvochem, England	
Ammonia solution NH <sub>3</sub>	NH <sub>4</sub> OH	25	Thomas Baker, India	
Ethylenediaminetetraacetic acid	$C_{10}H_{16}N_2O_8$	99	Alpha Chemika, India	
Isopropanol	C <sub>3</sub> H <sub>8</sub> O	70	Sigma-Aldrich, China	
<i>p</i> -Benzoquinone	$C_6H_4O_2$	98	Sigma-Aldrich, China	
Potassium dichromate	$K_2Cr_2O_7$	99	Thomas Baker, India	
Sodium oxalate	$Na_2C_2O_4$	99.5	Sigma-Aldrich, China	
Rhodamine B C <sub>28</sub> H <sub>31</sub> CIN <sub>2</sub> O <sub>3</sub>		Pure	Himedia	
dium metavanadate NH <sub>4</sub> VO <sub>3</sub>		99.9	Thomas Baker, India	
Hydrogen peroxide	vdrogen peroxide $H_2O_2$		Panreaca, China	
Hydrochloride acid HCL		35–38 Thomas Baker		



 $\textbf{Figure 1:} \ \ \text{Method of synthesizing metal ferrites Zn}_{0.5} \text{Mn}_{0.5} \text{Fe}_2 \text{O}_4 \ \ \text{nanocomposites}.$ 

In addition, hydrothermal synthesis was used to produce the  $Ag/AgVO_3$  nanoribbons. The standard operating procedure involves stirring the  $AgNO_3$  solution for 30 min. In the subsequent step, then adding  $NH_4VO_3$ , the suspension was stirred magnetically for 180 min to mix the components. The resulting

solution was placed in a stainless-steel autoclave lined with Teflon with a capacity of 100 m<sup>3</sup>. For 24 h, it remained hermetically closed at (180–200)°C in the oven. The washing and drying techniques were utilized in order to get the final component. Figures 2 and 3 show the synthesis of AgVO<sub>3</sub> and Ag/AgVO<sub>3</sub>.

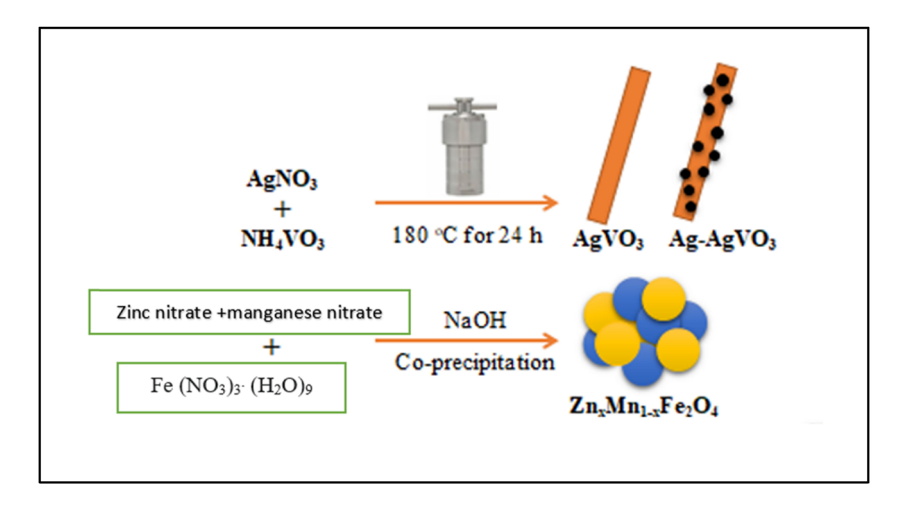
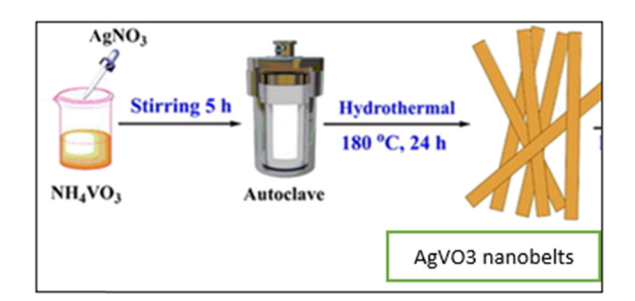


Figure 2: Procedure of the synthesis of AgVO<sub>3</sub>.



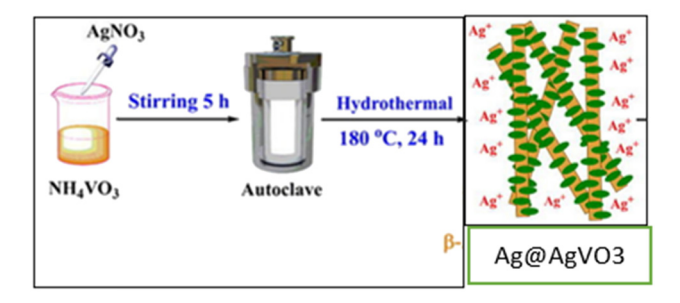


Figure 3: Procedure of the synthesis of AgVO<sub>3</sub> and Ag/AgVO<sub>3</sub>.

#### 2.4 Synthesis of Zn<sub>0.5</sub>Mn<sub>0.5</sub>Fe<sub>2</sub>O<sub>4</sub>/Ag/AgVO<sub>3</sub>

The Ag-silver vanadate samples were fabricated by a simple hydrothermal approach. For the synthesis of AgVO<sub>3</sub> nanoribbons, 2-25 mL solutions of AgNO3 and NH4VO3 in a molar ratio of 1:1 (each of 0.050 mol/L) were mixed for 20 min. Subsequently, the suspension that had been synthesized was stirred for 3 h. The resulting mixture was transferred into a hydrothermal reactor made of stainless steel with a volume of 100 mL. The reactor was equipped with a Teflon lining for insulation and was sealed tightly. The mixture was then subjected to a temperature of 180°C for 24 h. Subsequently, the reactor was set aside to undergo a progressive cooling process until it reached room temperature. Filtration and repeated washings with 100% ethanol and water helped to isolate the AgVO<sub>3</sub> sample. It was then vacuum dried at 80°C. The Ag-AgVO<sub>3</sub> sample was likewise synthesized using the same aforementioned method, with a molar ratio of 1.1 for AgNO<sub>3</sub>:NH<sub>4</sub>VO<sub>3</sub>.

 $Zn_xMn_{1-x}Fe_2O_4/AgVO_3$  and  $Zn_xMn_{1-x}Fe_2O_4/Ag-AgVO_3$  heterostructures were fabricated using coprecipitation of synthesized  $AgVO_3$  or  $Ag-AgVO_3$ . The molar ratio of the supported nanocomposite was specified (10% W of  $Zn_xMn_{(1-x)}Fe_2O_4$  and 90% W of  $Ag@AgVO_3$ ). A 0.1 g sample of  $AgVO_3$  or  $Ag-AgVO_3$  was sonicated in 20 mL of distilled water for 20 min. Aqueous solutions of iron(III) nitrate, manganese nitrate, and zinc nitrate were generated with appropriate molar ratios. These solutions were subsequently added to the  $AgVO_3$  or  $Ag-AgVO_3$  solution. The aforementioned combination was then heated to  $60^{\circ}C$  and

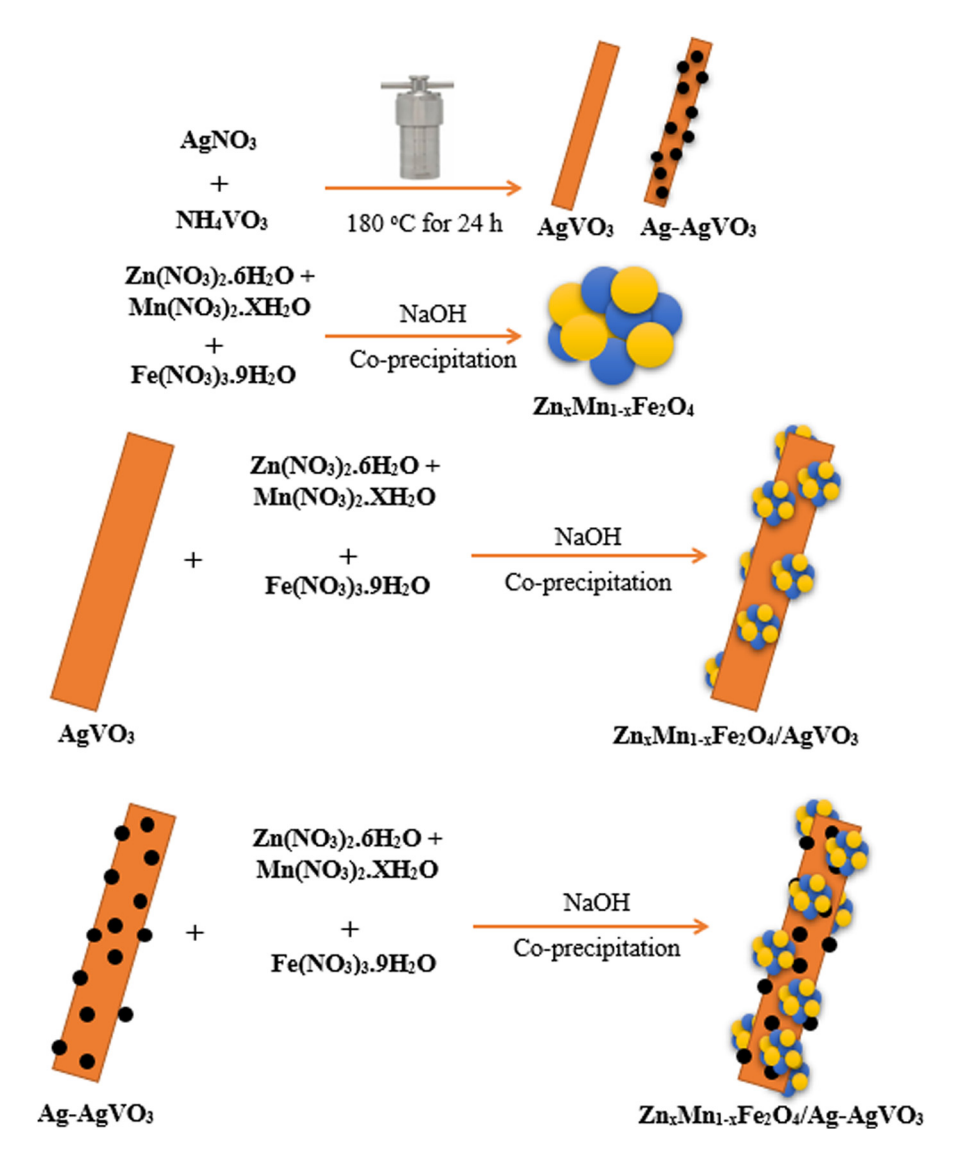
stirred. The pH of the solution was increased to approximately 12 with the addition of a 3 M NaOH solution. The settled  $Zn_xMn_{1-x}Fe_2O_4/AgVO_3$  or  $Zn_xMn_{1-x}Fe_2O_4/Ag-AgVO_3$  samples were separated, washed with a mixture of both water and alcohol and dried at 80°C. Scheme 1 shows the fabrication procedures of  $Zn_xMn_{1-x}Fe_2O_4/Ag/AgVO_3$  heterostructures.

# 2.5 Characterization of synthesized materials

Various techniques were used to characterize the recently synthesized photocatalysts, including X-ray diffraction (XRD), vibrating sample magnetometry (VSM), ultraviolet (UV)-visible diffuse reflectance spectroscopy, field emission scanning electron microscopy (FE-SEM), photoluminescence spectroscopy (PL), transmission electron microscopy (TEM), and BET analysis [31]. The XRD analysis was conducted at 25°C using a Shimadzu XRD-7000 instrument. The magnetic properties of the synthetic nanocomposite were assessed using VSM EZ7 with a field range of -10,000 to +10,000 Oe [32]. The study employed FE-SEM using the Tescan Mira 3 instrument to examine the morphological characteristics of the generated photocatalysts. The energy associated with the bandgap in these materials was examined using DRS, a technique employed to assess the extent of visible light absorption by photocatalysts [33]. The instrument used in the study was Hitachi U-3900H. The morphological characteristics and dimensions of the artificially produced nanoparticles were investigated using SEM. To examine the characteristics of ferrite metal nanocomposites, a BET analysis was conducted on individual nanoparticles [18,29]. The TEM was employed to examine the synthetic nanocomposites. The nanocomposites that were synthesized were likewise subjected to PL testing.

#### 2.6 Photocatalytic degradation experiments

Different samples (AgVO<sub>3</sub>, Ag/AgVO<sub>3</sub>, Zn<sub>0.5</sub>Mn<sub>0.5</sub>Fe<sub>2</sub>O<sub>4</sub>, and Zn<sub>0.5</sub>Mn<sub>0.5</sub>Fe<sub>2</sub>O<sub>4</sub>/Ag/AgVO<sub>3</sub>) were tested for their ability to function as photocatalysts in a visible light reactor. The evaluation was conducted through a batch photocatalytic degradation experiment, including the degradation of Rh B dye. A visible light source was directed into the photocatalytic reactor, which consisted of a glass beaker with a volume of 100 mL [34]. The visible lighting system comprises a pair of 35-watt Xenon lamps, two 30-watt lightemitting diode (LED) lights, and an additional pair of LED lights. The suspension of the photocatalyst was maintained



**Scheme 1:** Assembly procedure of Zn<sub>x</sub>Mn<sub>1-x</sub>Fe<sub>2</sub>O<sub>4</sub>/Ag-AgVO<sub>3</sub> nano-heterostructures.

by using a mixer, which effectively ensured the homogeneous blending of the various components within the reactor [20,35]. The photocatalytic degradation of Rh B began by introducing a 100-mL volume of Rh B dye to an aqueous solution with an initial concentration of 20 ppm. Subsequently, dosages of various nanocomposites were introduced to the solution at a concentration of 1g/L. The resulting mixture was stirred for 180 min, allowing it to attain a condition of absorption–desorption equilibrium. The reactor was exposed to light for a duration of 3 h, subsequent to being agitated for a total of 180 min. A UV-spectrometer (UV1200-Spectrophotometer) with a wavelength of 553 nm was used to collect a 3 mL sample every 5 minutes. Figure 6 depicts a schematic illustration of the photocatalytic degradation process of

Rh B dye as conducted in this experimental study. Additional factors that were investigated for their impact were the concentration of the photocatalyst, the initial concentration of Rh B dye, the initial pH level of the solution, and the concentration of  $H_2O_2$ . In order to assess their durability and potential for reuse, the metal ferrites produced in previous studies were subjected to a series of five photocatalytic degradation cycles [21,36]. Following each iteration, the catalyst was extracted from the reaction solution and washed three times with ethanol before being used again. Figure 4 illustrates the schematic representation of the batch reactor employed in the experimental study. Figure 5 illustrates the process of degradation efficiency under VLI.

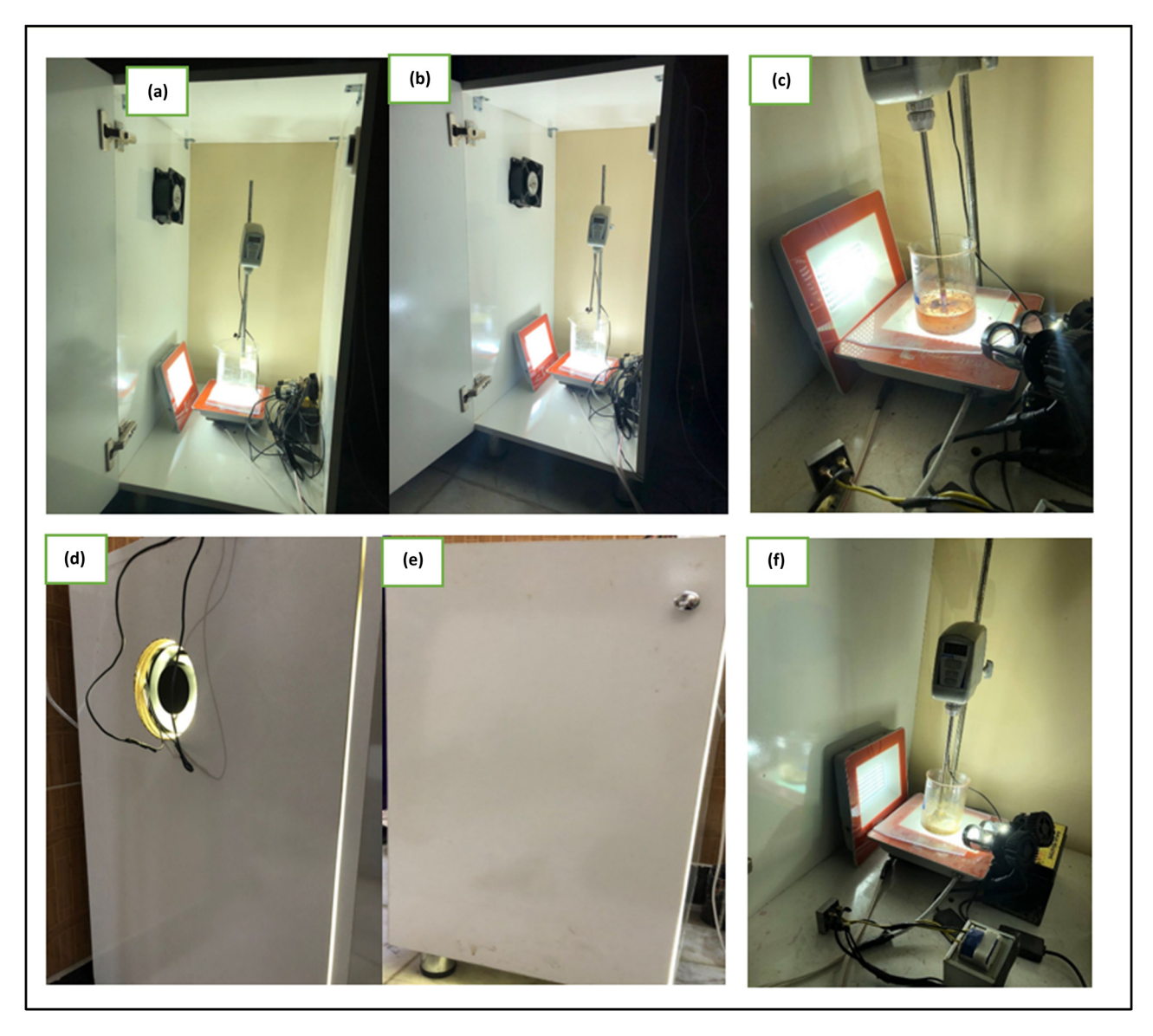


**Figure 4:** A schematic representation of a photocatalytic batch reactor system designed for the degradation of (Rh B) dye using VLI: (a)–(c) display the parts of the reactor inside the block, while (d) presents the part side, (e) shows the front part, and (f) shows the inside of the batch reactor.

### 3 Results and discussion

#### 3.1 Composition properties

Figure 6 shows that pure Ag/AgVO<sub>3</sub> and AgVO<sub>3</sub> have diffraction peaks at  $2\theta = 19.1^{\circ}$ ,  $24.3^{\circ}$ ,  $29.6^{\circ}$ ,  $31.7^{\circ}$ ,  $33.3^{\circ}$ ,  $37.1^{\circ}$ ,  $39.5^{\circ}$ ,  $45.4^{\circ}$ ,  $51.3^{\circ}$ ,  $55.3^{\circ}$ , and  $60^{\circ}$ , as well as  $12.4^{\circ}$ ,  $17.1^{\circ}$ ,  $25.1^{\circ}$ ,  $27.4^{\circ}$ ,  $28.1^{\circ}$ , $29.7^{\circ}$ ,  $31.2^{\circ}$ ,  $32.7^{\circ}$ ,  $33.3^{\circ}$ , and  $34.6^{\circ}$ . Based on these results, the initial phases of Ag/AgVO<sub>3</sub> and AgVO<sub>3</sub> are tetragonal (JCPDS No. 10-0445) and monoclinic (JCPDS No. 89-4396), respectively [37]. Based on the data presented in Figure 6, it can be inferred that the peak intensities associated with Ag/AgVO<sub>3</sub> exhibit a gradual augmentation as AgVO<sub>3</sub> is introduced. In

addition, because  $AgVO_3$  makes up such a small percentage of  $Zn_{0.5}Mn_{0.5}Fe_2O_4/Ag/AgVO_3$  nanocomposite photocatalysts, the typical peaks of  $AgVO_3$  cannot be found in these materials. In conclusion, the absence of any other peaks in the nanocomposite, which confirmed the complete absence of impurities in the as-prepared photocatalysts [29], was observed. Crystalline size values were determined for pure  $AgVO_3$ , and  $Zn_{0.5}Mn_{0.5}Fe_2O_4/Ag/AgVO_3$  nanocomposites, and those results are displayed in Figure 7. In this particular scenario, an augmentation in the quantity of  $AgVO_3$  leads to a diminution in the crystalline dimensions of the composite material. The utilization of XRD was employed for the purpose of examining the structure and composition of the

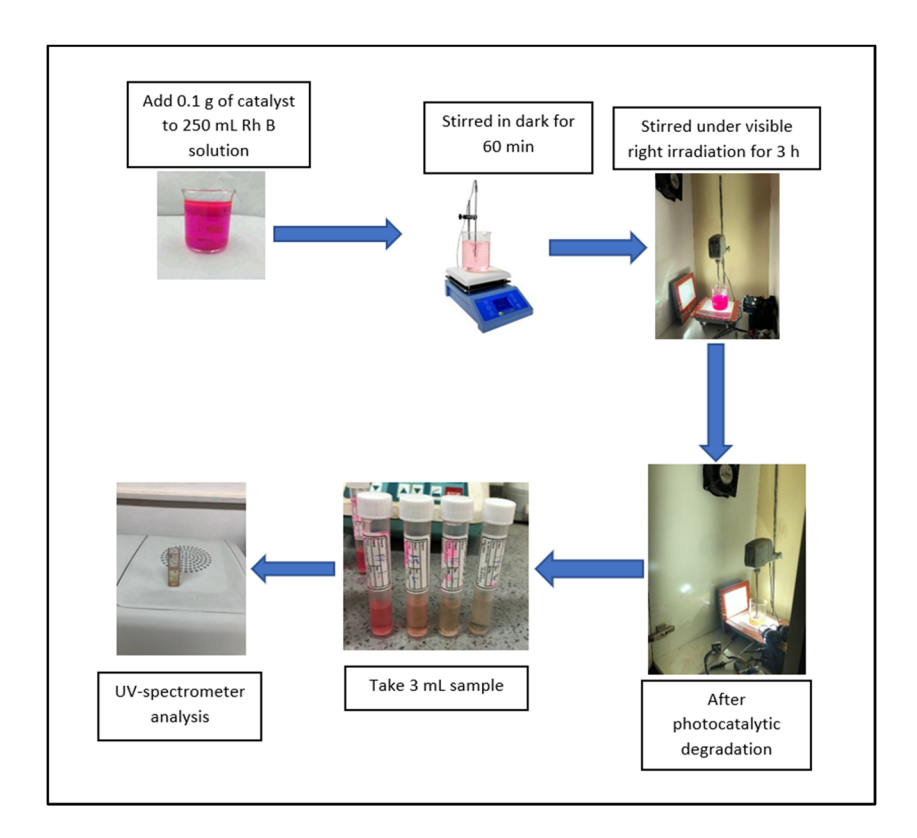


Figure 5: Procedural steps involved in the photocatalytic degradation of (Rh B) dye using a visible light source.

sample [38,39]. Figure 6 illustrates a comparison between the XRD spectra of two types of silver agvorite: Ag–AgVO $_3$  and Zn $_{0.5}$ Mn $_{0.5}$ Fe $_2$ O $_4$ /Ag/AgVO $_3$ . The crystal structure of monoclinic beta-AgVO $_3$  is characterized by the diffraction peak observed in the sample, as documented in the JCPDS card 29-1154. The plane corresponding to the characteristic diffraction peak 501 of AgVO $_3$  is determined at 30.0° [40].

The diffraction peaks of Ag (111), Ag (200), Ag (220), and Ag (311) were observed in face-centered cubic structures retrieved at 38.1°, 44.8°, 63.9°, and 77.1°. The locations of the peaks of the synthesized Ag–AgVO $_3$  may be shown to be almost identical to those of the  $\rm Zn_{0.5}Mn_{0.5}Fe_2O_4/Ag/AgVO_3$  compound, as can be seen in Figure 7. At an angle of 28.6°, a difference in the peaks of the diffraction pattern can be seen. It is the shift that occurred as a result of the incorporation of Ag.

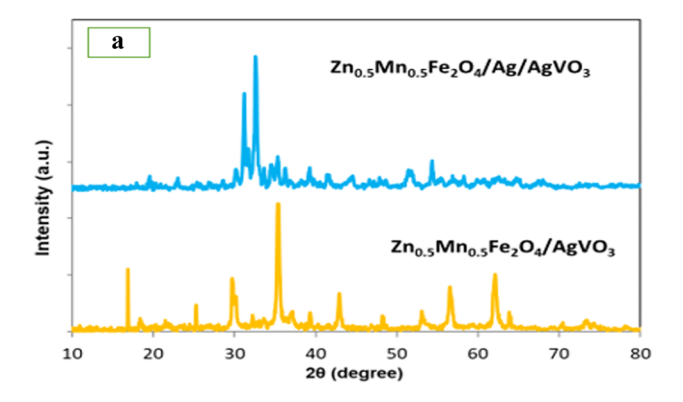
#### 3.2 Magnetic properties

The synthetic  $Zn_{0.5}Mn_{0.5}Fe_2O_4/Ag/AgVO_3$  were analyzed and compared to those of individual  $Zn_{0.5}Mn_{0.5}Fe_2O_4/AgVO_3$  and  $Zn_{0.5}Mn_{0.5}Fe_2O_4$ . Nanocomposite magnetization is shown in Figure 7; the  $Zn_{0.5}Mn_{0.5}Fe_2O_4/Ag/AgVO_3$  sample has a low

magnetization saturation (MS) value of  $0.25 \, \text{emu/g}$ , whereas the  $\text{ZnFe}_2\text{O}_4$  sample has a high value (3.5 emu/g). The magnetization of a  $\text{Zn}_{0.5}\text{Mn}_{0.5}\text{Fe}_2\text{O}_4$  sample is just 1.5 emu/g. Nanocomposite magnetization is  $0.25 \, \text{emu/g}$ , which is notably lower in comparison to the values exhibited by other materials. However, the field strength used was between 15,000 and 15,000 Oe [41].

#### 3.3 Morphological analysis

The FE-SEM pictures of the synthetic supported nanocomposite are shown in Figure 8.  $Zn_{0.5}Mn_{0.5}Fe_2O_4$  magnetic metal ferrites have a rough surface and spherical nanoparticles with sizes between 37.96 and 55.82 nm based on morphological analysis. Microsphere-shaped clusters with dimensions between 17.86 supported nanocomposite, disclosing AgVO\_3@Ag attached on the metal ferrite thought to be the core, a layer of silver vanadate attached to metal ferrite, and the Ag ion distributed on the silver vanadate as the final layer. The nanocomposite is shown in Figure 9. Supported  $Zn_{0.5}Mn_{0.5}Fe_2O_4/Ag/AgVO_3$  are the most obvious type of nanocomposite. The supported hybrid might be as small as 45.42 nm or as large as 20.33 nm. The nanocomposite surface contained



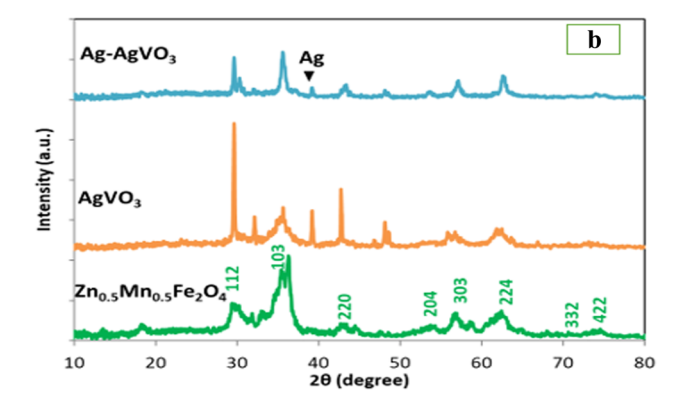


**Figure 6:** (a) XRD patterns of AgVO<sub>3</sub>, Ag–AgVO<sub>3</sub>, and  $Zn_{0.5}Mn_{0.5}Fe_2O_4$ . (b) XRD patterns of  $Zn_{0.5}Mn_{0.5}Fe_2O_4$ @AqVO<sub>3</sub> and  $Zn_{0.5}Mn_{0.5}Fe_2O_4$ /Aq/AqVO<sub>3</sub>.

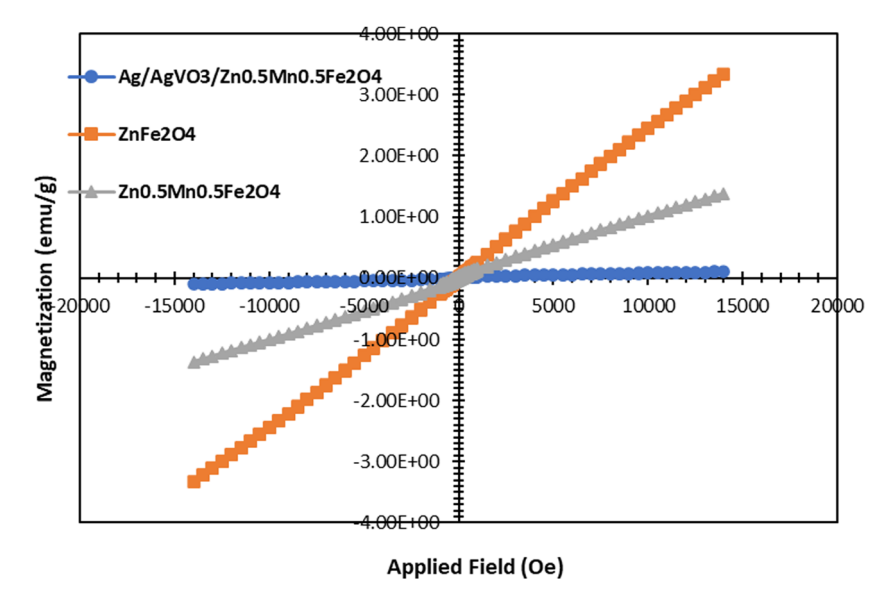
tiny zinc and manganese nanoparticles. The EDS analysis of the nanocomposites is illustrated in Figure 10 in which each of  $AgVO_3$ ,  $Ag/AgVO_3$ , and the supported  $Zn_0 SMn_0 SFe_2O_4/Ag/Se_2O_5/Ag/Se_2O_5/A$ 

AgVO<sub>3</sub> nanocomposites represent the chemical composition for all the elements presented in the nanoparticles [42].

#### 3.4 UV-vis-DRS analysis

The typical DRS spectra of magnetic nanoparticles are shown in Figure 9: Zn<sub>0.5</sub>Mn<sub>0.5</sub>Fe<sub>2</sub>O<sub>4</sub>, Ag/AgVO<sub>3</sub>, Zn<sub>0.5</sub>Mn<sub>0.5</sub>Fe<sub>2</sub>O<sub>4</sub>/Ag/AgVO<sub>3</sub>, and Zn<sub>0.5</sub>Mn<sub>0.5</sub>Fe<sub>2</sub>O<sub>4</sub>/AgVO<sub>3</sub>. The formation of "heteroconnection between the two semiconductors" in Zn<sub>0.5</sub>Mn<sub>0.5</sub>Fe<sub>2</sub>O<sub>4</sub>/Ag/ AgVO<sub>3</sub> increased the visible light absorption limits. These results explain how visible light can improve the photocatalytic activity of a photocatalyst, mainly by creating more electron-hole pairs. The determination of the bandgap energy (E<sub>g</sub>) of the synthesis-supported Zn<sub>0.5</sub>Mn<sub>0.5</sub>Fe<sub>2</sub>O<sub>4</sub>/Ag/ AgVO<sub>3</sub> nanocomposite, as well as the analytical findings from the DRS technique, was achieved using the Kubelka-Muk relation (Equation (1)) [43]. Equation (1) denotes "the absorption coefficient, photon frequency, plank constant, the destiny of transition, incident light frequency, and the proportionality constant" with the symbols "v, h, n, and A." Figure 11 displays the calculated bandgaps in eV for each element. Zn<sub>0.5</sub>Mn<sub>0.5</sub>Fe<sub>2</sub>O<sub>4</sub> and Zn<sub>0.5</sub>Mn<sub>0.5</sub>Fe<sub>2</sub>O<sub>4</sub>/Ag/AgVO<sub>3</sub> have been measured to have bandgap energies of 3 and 1.5 eV, respectively. The supported Zn<sub>0.5</sub>Mn<sub>0.5</sub>Fe<sub>2</sub>O<sub>4</sub>/Ag/ AgVO<sub>3</sub> exhibits a reduced bandgap energy, resulting in a higher generation of electron/hole (e<sup>-</sup>/h<sup>+</sup>) pairs compared to other samples [12,42,44]

$$\alpha h \nu = A(h \nu - E_{\sigma})^{n/2}. \tag{1}$$



 $\textbf{Figure 7:} \ \ \text{Magnetic hysteresis curves of synthesized } \ \ \text{Zn}_{0.5} \\ \text{Mn}_{0.5} \\ \text{Fe}_2 \\ \text{O}_4 \\ \text{Ag/Ag/O}_3 \ \text{samples at room temperature.}$ 

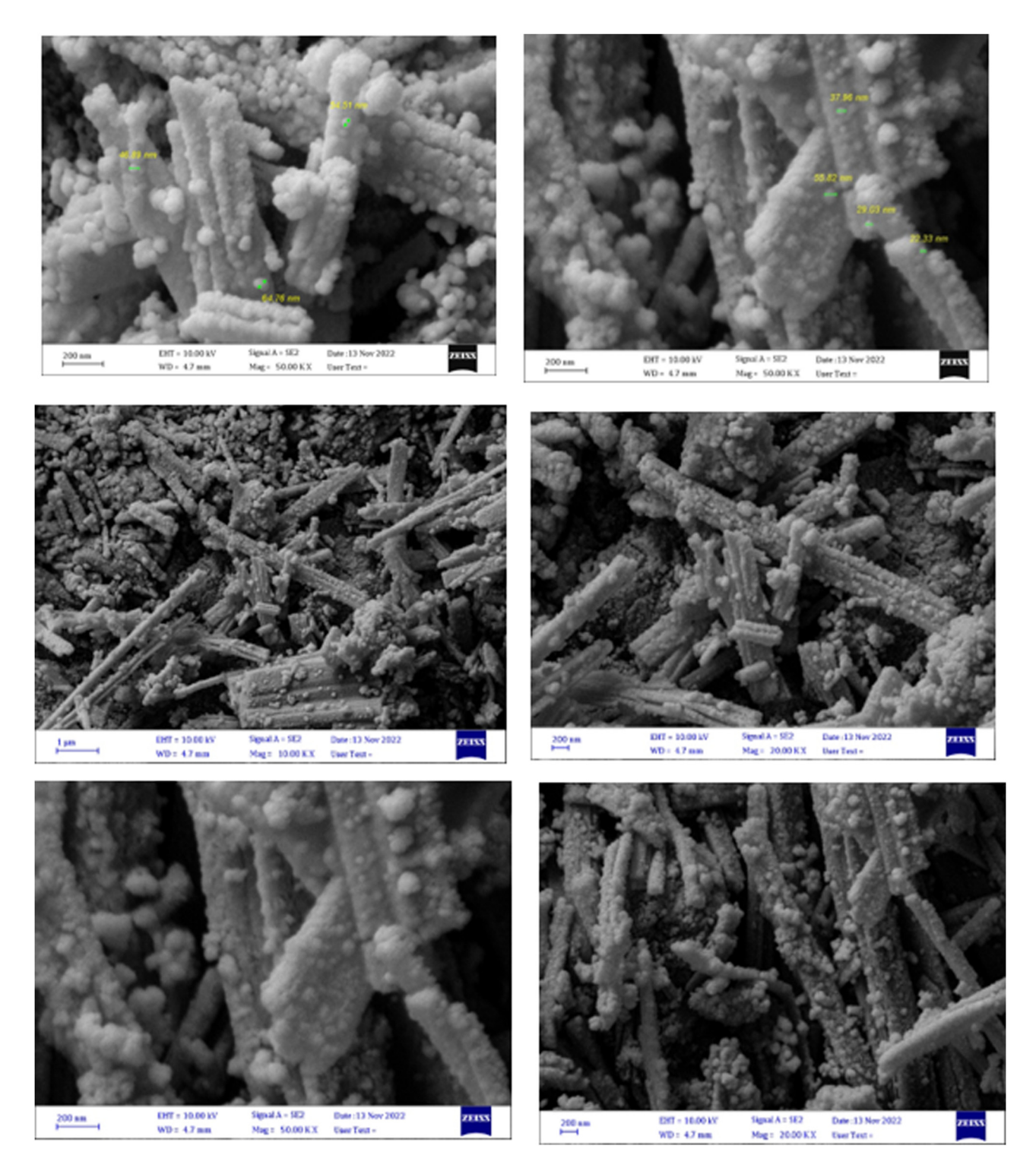
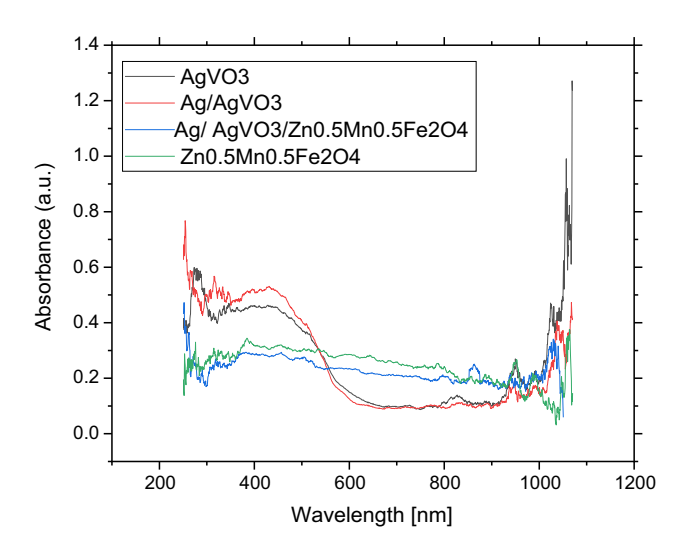


Figure 8: FE-SEM images of synthesized nanocomposite Zn<sub>0.5</sub>Mn<sub>0.5</sub>Fe<sub>2</sub>O<sub>4</sub>/Ag/AgVO<sub>3</sub>.

#### 3.5 Surface properties

Using adsorption-desorption isotherm curves, the nanocomposite's porosity and surface area distribution were studied [45]. Type IV sorption is characteristic of mesoporous materials, and all four showed a similar hysteresis loop at quite high pressures of ft. While the adsorption—desorption isotherms for  $AgVO_3$  ranged from 0.5 to 40, those for  $Ag@AgVO_3$  ranged from 0.5 to 30, for the supported nanocomposites ranged from 0.5 to 27, and the metal ferrites



**Figure 9:** DRS analysis for nanocomposite: (a) AgVO<sub>3</sub>, (b) Ag@AgVO<sub>3</sub>, (c) AgVO<sub>3</sub>/Zn<sub>0.5</sub>Mn<sub>0.5</sub>Fe<sub>2</sub>O<sub>4</sub>, (d) Zn<sub>0.5</sub>Mn<sub>0.5</sub>Fe<sub>2</sub>O<sub>4</sub>/Ag/AgVO<sub>3</sub>, and (e) Zn<sub>0.5</sub>Mn<sub>0.5</sub>Fe<sub>2</sub>O<sub>4</sub>.

ranged from 0.5 to 150. The Barrett-Joyner-Halenda method further demonstrated the irregularity of the photocatalyst's mesopores through the measurement techniques employed for determining the distribution of pore sizes and the movement of the looping procedure at high relative pressures  $(P/P_0)$  within the range of 0.5–1.0 are examined [46]. Supported nanocomposites' ads-des isotherms varied between 0.5 and 20 K. There were larger holes in AgVO<sub>3</sub> and Ag@AgVO<sub>3</sub>, with sizes ranging from 17 to 22 nm. The  $S_{\text{BET}}$  values for AgVO<sub>3</sub>, Ag@AgVO<sub>3</sub>, and Zn<sub>0.5</sub>Mn<sub>0.5</sub>Fe<sub>2</sub>O<sub>4</sub>/Ag/AgVO<sub>3</sub> were 13.471, 10.047, and 5.5148 m<sup>2</sup>/g, respectively. Table 1 includes supplementary information about many parameters. These include the  $S_{tot}$ ,  $S_{\text{RET}}$ , pore volume  $(V_{\text{p}})$ , and pore diameter  $(D_{\text{p}})$ . The adsorption and desorption are depicted in Figures 12–15, respectively, and display the pore-size distribution map and nitrogen desorption adsorption isotherm for all nanocomposites.

The results of the specific surface area analysis indicate that the Zn<sub>0.5</sub>Mn<sub>0.5</sub>Fe<sub>2</sub>O<sub>4</sub>/Ag/AgVO<sub>3</sub> composite material exhibits a specific surface area of 4.3869 m<sup>2</sup>/g, while the Ag-AgVO<sub>3</sub> composite material demonstrates a specific surface area of 10.049 m<sup>2</sup>/g. Additionally, the metal ferrite material displays a specific surface area of 44.829 m<sup>2</sup>/g. The experimental results indicate that Zn<sub>0.5</sub>Mn<sub>0.5</sub>Fe<sub>2</sub>O<sub>4</sub> possesses a higher specific surface area in comparison to both Ag-AgVO<sub>3</sub> and Zn<sub>0.5</sub>Mn<sub>0.5</sub>Fe<sub>2</sub>O<sub>4</sub>/Ag/AgVO<sub>3</sub> composites. Based on the available data, it can be inferred that the specific surface area had a limited impact on the photocatalytic degradation process. The SEM figure reveals that the dispersion of the Zn<sub>0.5</sub>Mn<sub>0.5</sub>Fe<sub>2</sub>O<sub>4</sub> structure and the adhesive superposition of Ag-AgVO<sub>3</sub> result in a reduction in the specific surface area. When comparing Zn<sub>0.5</sub>Mn<sub>0.5</sub>Fe<sub>2</sub>O<sub>4</sub> to Ag–AgVO<sub>3</sub>, it can be observed that the former has a larger size, a lower specific

surface area, and a narrower distribution of pore sizes. In contrast, the latter has a significantly smaller size of approximately 3.5 nm and possesses a hole structure (Table 2).

#### 3.6 Photoluminescence

It is very important that photoexcited charge carriers are recombined efficiently because it affects the photocatalysts process. The fluorescence emission intensity decreases as the distance between the charge carriers increases. The PL spectra at an excitation wavelength of 320 nm, as shown in Figure 16, correspond to three different samples: pure  $AgVO_3$ ,  $Ag-AgVO_3$ , and a nanocomposite consisting of  $Zn_{0.5}Mn_{0.5}Fe_2O_4/Ag/AgVO_3$ .

In addition, it was noted that the  $Zn_{0.5}Mn_{0.5}Fe_2O_4/Ag/Ag/O_3$  nanocomposite photocatalyst has a lower intensity than both pure for  $AgVO_3$  and  $Ag@AgVO_3$ , verifying the composite's low rate of recombination. This means that the nanocomposite is more effective than pure  $AgVO_3$  and  $Ag@AgVO_3$  at separating electron and hole pairs. The photocatalytic efficiency of photocatalysts in their original state depends a lot on how well photoexcited charge carriers can combine back together. Furthermore, previous studies have demonstrated that the photocatalytic efficiency of the supported  $Zn_{0.5}Mn_{0.5}Fe_2O_4/Ag/AgVO_3$  nanocomposite was improved because of the decreased recombination of charge carriers.

The examination of PL spectra allows for the elucidation of transfer and separation efficiency of charge carriers created by light in semiconductor materials [40]. The increase in photocatalytic activity is caused by additional electrons and holes participating in oxidation and reduction reactions [47]. This is shown by a lower PL intensity, which means that charge carriers are recombining less [48].

As individuals move further apart from each other, there is a decrease in the intensity of their fluorescence emission [29]. The PL spectra at an excitation wavelength of 320 nm, as depicted in Figure 17, correspond to three distinct samples: pure AgVO<sub>3</sub>, Ag@AgVO<sub>3</sub>, and a nanocomposite consisting of Zn<sub>0.5</sub>Mn<sub>0.5</sub>Fe<sub>2</sub>O<sub>4</sub>/Ag/AgVO<sub>3</sub>.

The primary emission peak in the visible light range, approximately at a wavelength of 796.9799 nm, can be attributed to the recombination of electron–hole pairs within the band gap. The relative intensity of the composite material consisting of supported  $\rm Zn_{0.5}Mn_{0.5}Fe_2O_4/Ag/AgVO_3$  is found to be weaker compared to that of pure AgVO\_3 and Ag@AgVO\_3. This suggests that the charge transfer occurring between  $\rm Zn_{0.5}Mn_{0.5}Fe_2O_4$  and Ag/AgVO\_3 formed on its surface is highly efficient, effectively inhibiting the recombination of

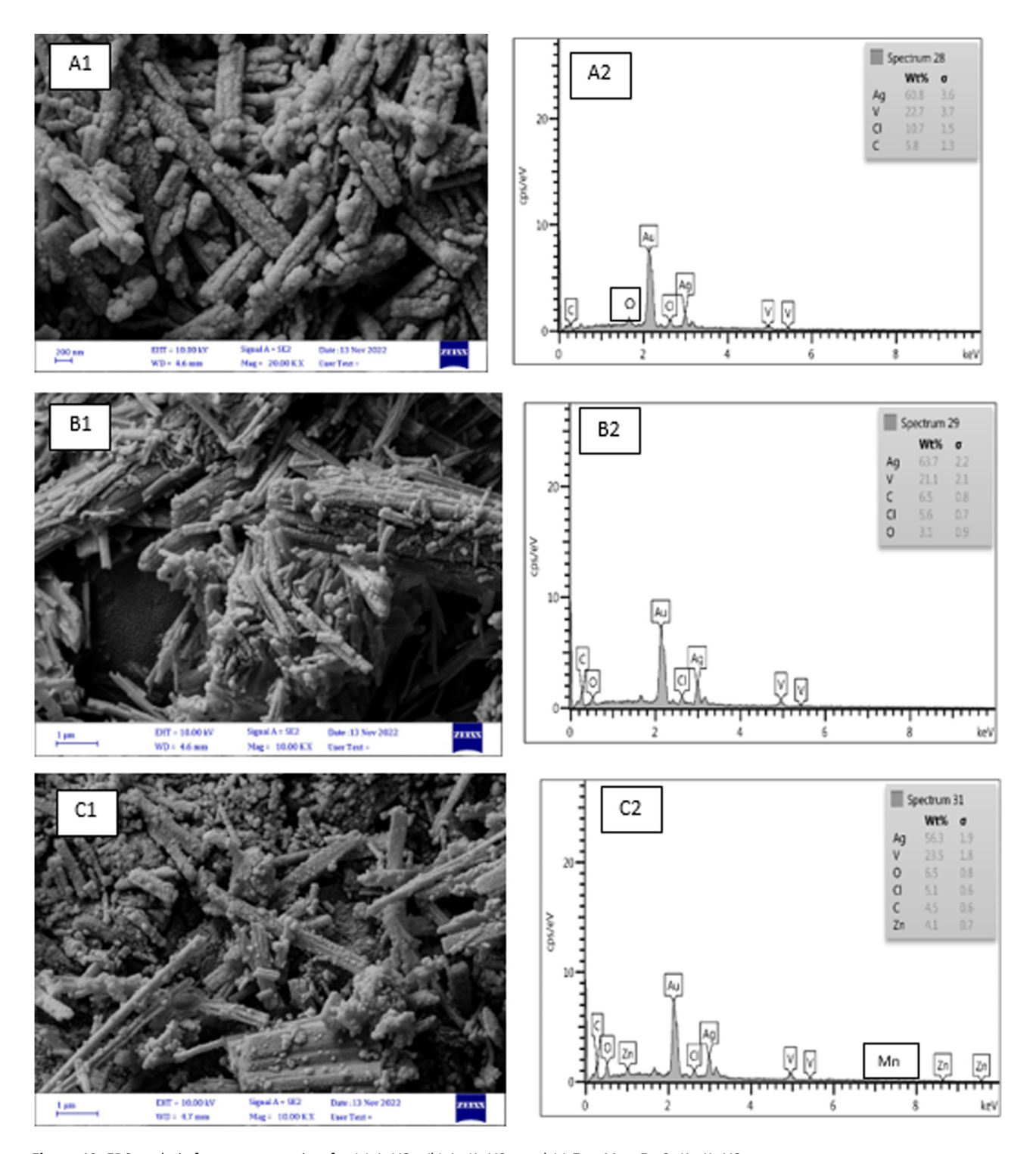


Figure 10: EDS analysis for nanocomposites for (a)  $AgVO_3$ , (b)  $Ag/AgVO_3$ , and (c)  $Zn_{0.5}Mn_{0.5}Fe_2O_4/Ag/AgVO_3$ .

electrons and holes. One crucial factor in improving the degradation of Rh B is the inhibition of electron-hole pair recombination [29]. The findings indicate that a composite material consisting of Zn<sub>0.5</sub>Mn<sub>0.5</sub>Fe<sub>2</sub>O<sub>4</sub> supported on Ag/ AgVO<sub>3</sub>, when appropriately proportioned, exhibits notable efficacy.

#### 3.7 TEM analysis

The claviform shape and dense coating of tiny particles on the surface of Ag-AgVO<sub>3</sub> are clearly visible in Figure 18. Nanorods are typically 50 nm thick and 100 nm wide [49]. The identification of minute particles adhering to the

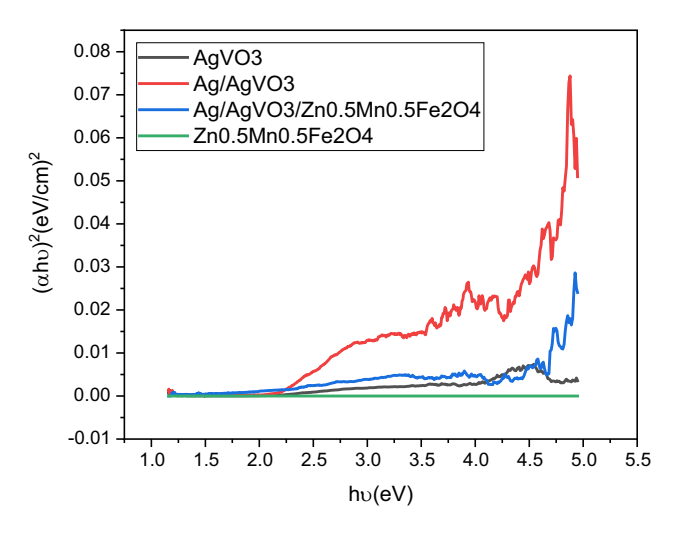


Figure 11: Bandgap evaluation for  $Zn_{0.5}Mn_{0.5}Fe_2O_4$ ,  $AgVO_3$ ,  $Ag@AgVO_3$ , and  $Zn_{0.5}Mn_{0.5}Fe_2O_4/Ag/AgVO_3$ .

surface has conclusively determined them to be composed of silver (Ag) [50]. The  $\rm Zn_{0.5}Mn_{0.5}Fe_2O_4/Ag/AgVO_3$  composite exhibits distinct crumpled and creased layered structures, reminiscent of gauze, which aligns with the characteristic lamellar structural features observed in metal ferrite materials. The core/shell structure of  $\rm Zn_{0.5}Mn_{0.5}Fe_2O_4$  contrasts with the one-dimensional (1D) structure of Ag–AgVO $_3$ . 1D structures can be combined with 1D structures to produce a network structure that enhances the material's physical and chemical properties [51]. As depicted in Figure 17, there is a notable decline in the adhesion between nanorods. The 0.24 nm crystal spacing is confirmed to be Ag particles by

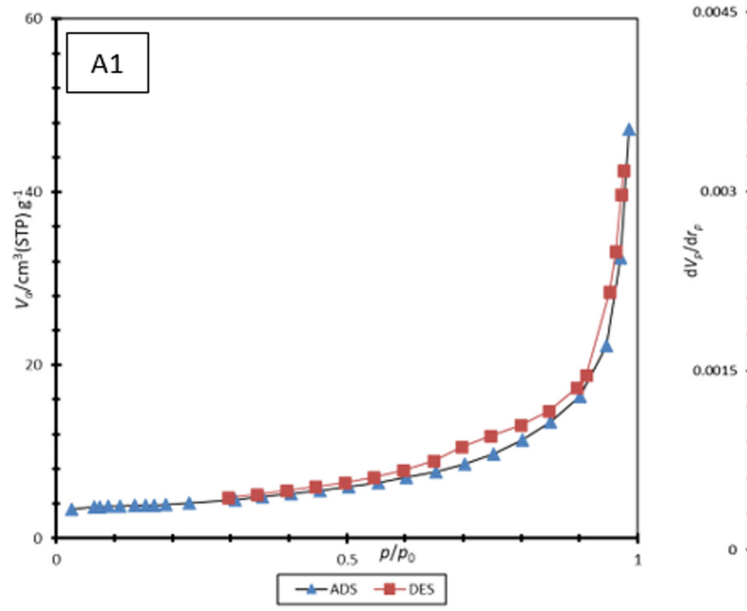
TEM observation, which is depicted in Figure 18. The crystal spacing observed in this case is consistent with the Ag (111) crystal plane. The distance between the two nano rods is roughly 100 nm, as shown in Figure 18. Moreover, the gap quickly shrinks to around 20 nm with the addition of  $Zn_{0.5}Mn_{0.5}Fe_2O_4$ . The results indicate that  $Zn_{0.5}Mn_{0.5}Fe_2O_4$  was successfully deposited on the surface of AgVO<sub>3</sub> nano rods.

The aforesaid results, when taken together with the XRD and SEM, demonstrate that  $Zn_{0.5}Mn_{0.5}Fe_2O_4/Ag/AgVO_3$  has been successfully prepared. Figure 17 displays a histogram illustrating the diameter distribution of Ag and AgVO $_3$  quantum dots as measured by TEM.

#### 3.8 Photocatalytic destruction performance

The degradation of Rh B was employed as a means to evaluate the efficacy of photocatalytic reactions exhibited by the photocatalysts that were synthesized and demonstrated activity under visible light [52]. After 90 min of irradiation, Rh B shows no significant change in a photodegradation experiment without a catalyst, demonstrating that it is not degradable. Compared to pure  $\rm Zn_{0.5}Mn_{0.5}Fe_2O_4/Ag/AgVO_3$  nanocomposites exhibit greater degrading efficiency under VLI (Figure 18).

When comparing the photocatalytic activity of the nanocomposites,  $Zn_{0.5}Mn_{0.5}Fe_2O_4/Ag/AgVO_3$  had the highest activity (99.99%), followed by  $Zn_{0.3}Mn_{07}Fe_2O_4/AgVO_3$  (90%),



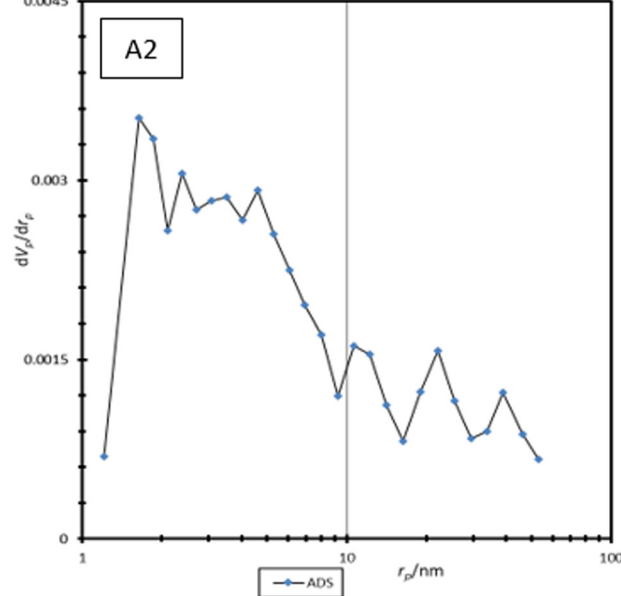


Figure 12: Adsorption-desorption for AgVO<sub>3</sub> and the pore size for AgVO<sub>3</sub>.

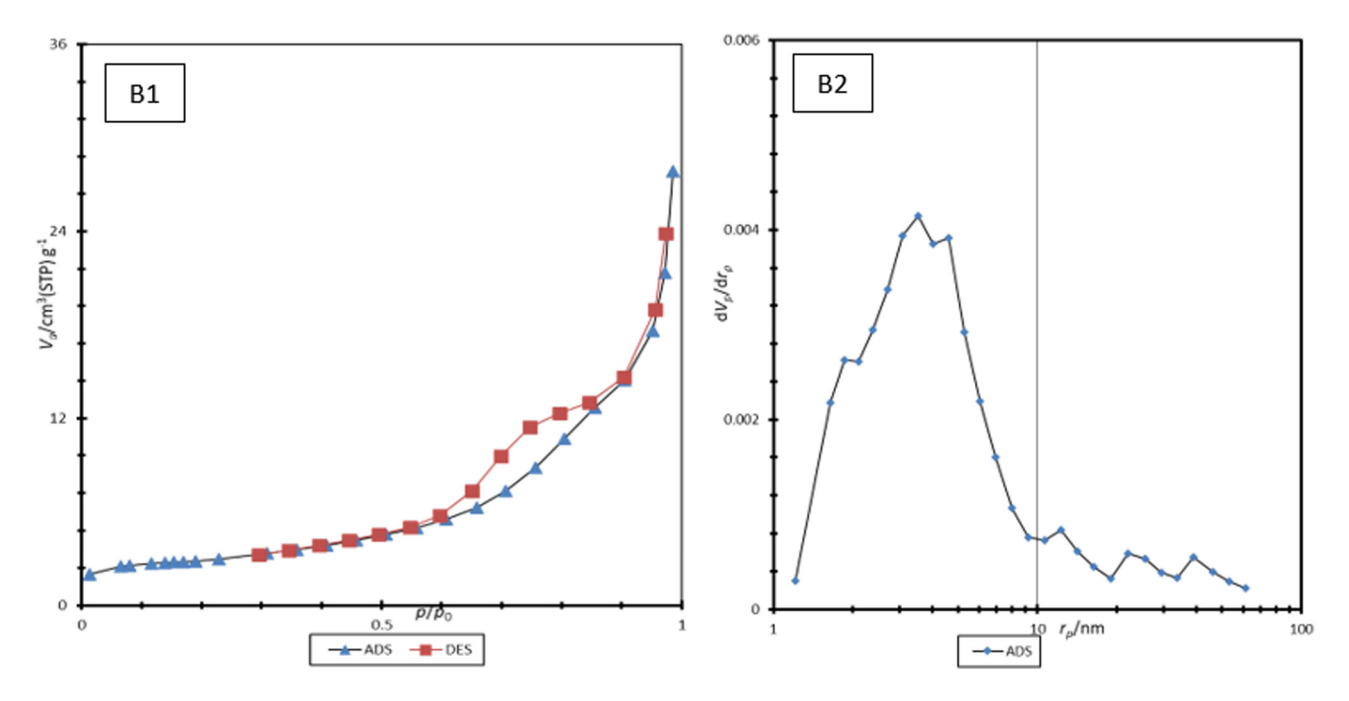
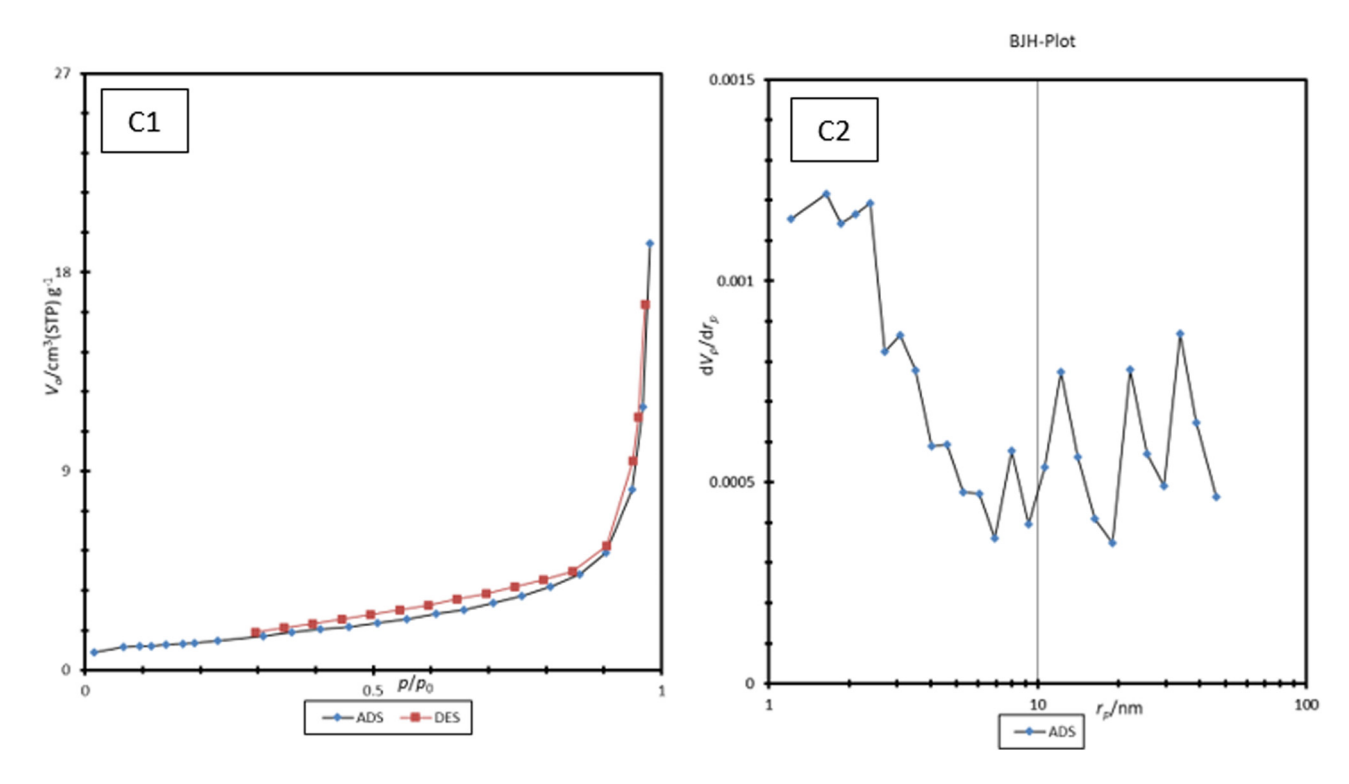


Figure 13: ads-des for Ag/AgVO<sub>3</sub> nanocomposite.

and  $Zn_{0.5}Mn_{0.5}Fe_2O_4/AgVO_3$  (80%). The catalytic efficiency was found to be influenced by the  $AgVO_3$  composition, with an increase in  $AgVO_3$  loadings in the  $Zn_{0.5}Mn_{0.5}Fe_2O_4/Ag/AgVO_3$  nanocomposites leading to a decrease in catalytic activity. Therefore, the superiority of the active hetero-

interfaces of the  $Zn_{0.5}Mn_{0.5}Fe_2O_4/Ag/AgVO_3$  nanocomposites was diminished by the addition of a small amount of  $Zn_{0.5}Mn_{0.5}Fe_2O_4$  and facilitated the enhancement of charge transfer across the surfaces of the heterojunction [17,53].



 $\textbf{Figure 14:} \ \ \text{ads-des (adsorption-desorption) process and pore size for } \ \ Zn_{0.5}Mn_{0.5}Fe_2O_4/Ag/AgVO_3 \ \ \text{nanocomposite}.$ 

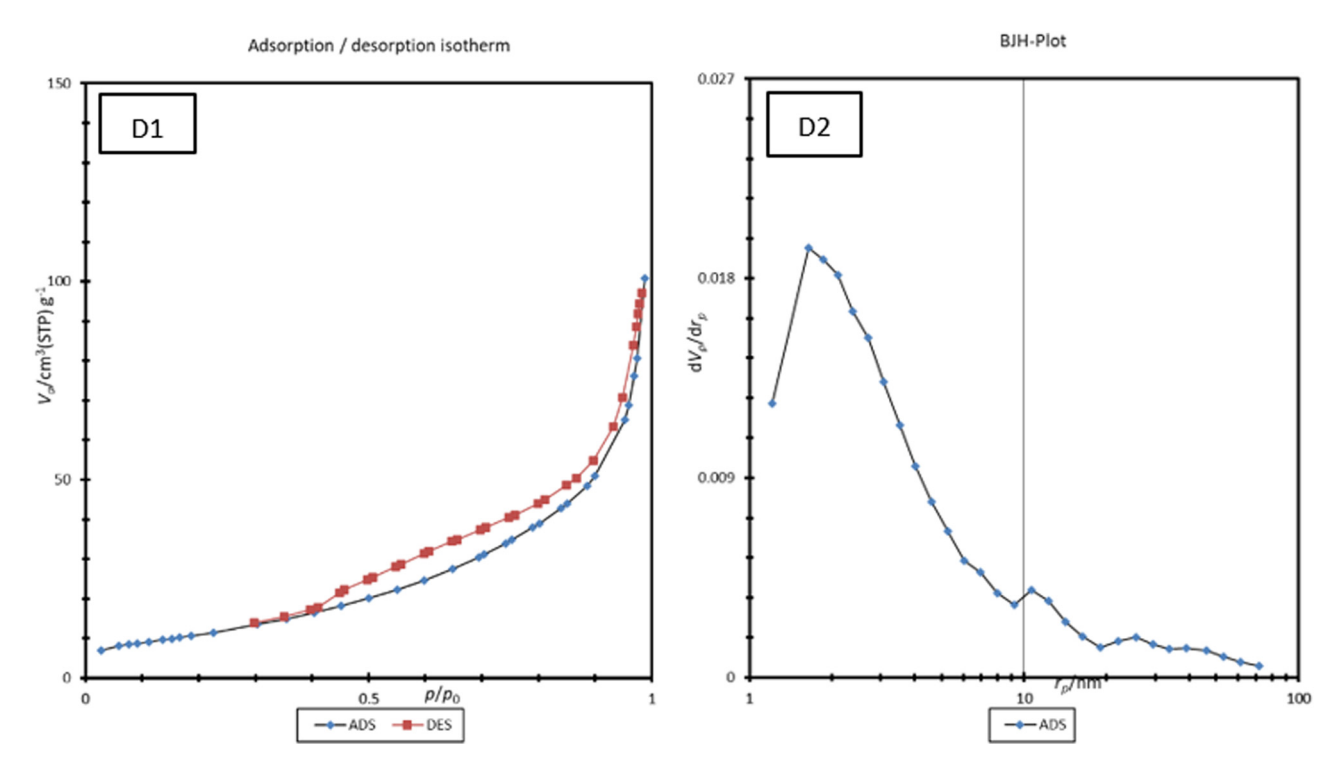


Figure 15: ads-des process and the pore size for Zn<sub>0.5</sub>Mn<sub>0.5</sub>Fe<sub>2</sub>O<sub>4</sub>.

Applying the following "pseudo-first-order kinetics equation" [54,55], there were able to gain a quantitative understanding of the reaction kinetics [56]:

$$K_{t} = -\ln(C_0/C_t). \tag{2}$$

The initial Rh B concentration,  $C_0$ , and the final Rh B concentration,  $C_b$  along with the reaction rate constant, k, and the irradiation period, t, in minutes, are shown in the equation (2) [57]. The degradation of Rh B followed pseudo-first-order kinetics [58], as indicated by the linear relationship between degradation and time, as shown in Figure 19. It shows that compared to pure  $Zn_{0.5}Mn_{0.5}Fe_2O_4$ ,  $AgVO_3$ ,  $Ag/AgVO_3$ , the rate constant (k) value for  $Zn_{0.5}Mn_{0.5}Fe_2O_4/Ag/AgVO_3$  nanocomposite photocatalysts is significantly greater. When compared to pure  $Zn_{0.5}Mn_{0.5}Fe_2O_4$ , the rate constant value of  $Zn_{0.5}Mn_{0.5}Fe_2O_4/Ag/AgVO_3$  is roughly 4 and 7.5 times higher.

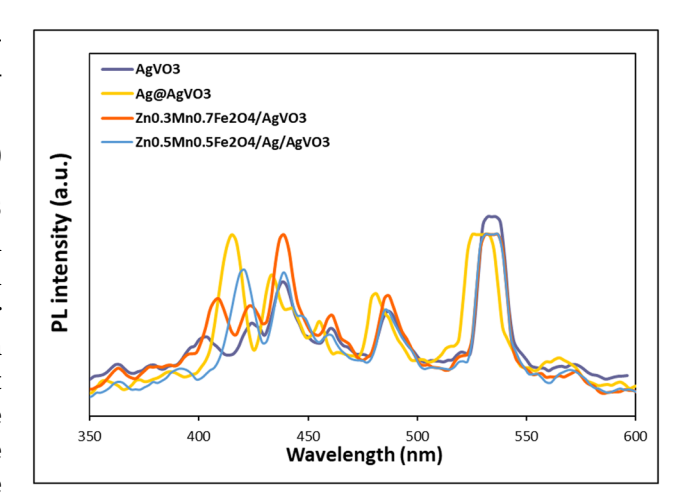


Figure 16: PL analysis for supported nanocomposites.

Table 2: Surface properties of the supported nanocomposites

Sample	a <sub>s,BET</sub> (m <sup>2</sup> /g)	V <sub>p</sub> (cm³/g)	r <sub>p,peak</sub> (nm)	Average pore diameter (nm)	Total pore volume $(p/p_0 = 0.981)$ $(cm^3/g)$		
AgVO <sub>3</sub>	13.471	0.0674	1.64	21.703	0.073089		
Ag-AgVO <sub>3</sub>	10.049	0.04298	3.53	17.142	0.043065		
Zn <sub>0.5</sub> Mn <sub>0.5</sub> Fe <sub>2</sub> O <sub>4</sub> Aq-AqVO <sub>3</sub> /Zn <sub>0.5</sub> Mn <sub>0.5</sub> Fe <sub>2</sub> O <sub>4</sub>	44.829 4.3869	0.1563 0.029413	1.64 1.64	13.906 27.212	0.1559 0.029844		

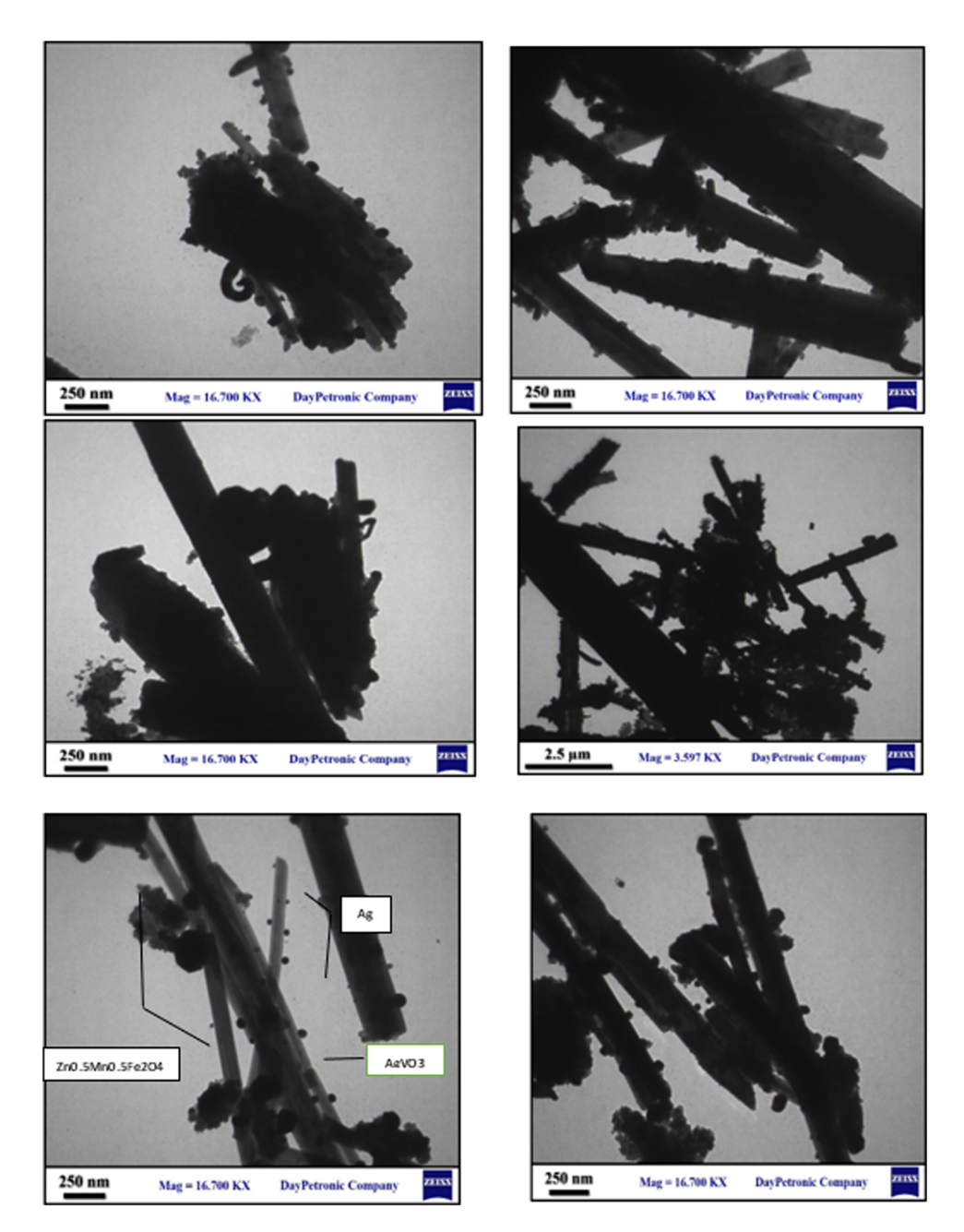


Figure 17: TEM images for the Zn<sub>0.5</sub>Mn<sub>0.5</sub>Fe<sub>2</sub>O<sub>4</sub>/Ag/AgVO<sub>3</sub> nanocomposites.

From 1 g/L of the improved  $Zn_{0.5}Mn_{0.5}Fe_2O_4/Ag/AgVO_3$  catalyst was tested for its influence on Rh B degradation in the presence of VLI. As depicted in Figure 18, the photocatalytic degradation capacity exhibits a steady increase until reaching a concentration of 1.5 g/L, after which it gradually declines. The degradation rate exhibited an initial increase due to the greater availability of active sites inside the photocatalyst. However, as the dose of catalyst employed was increased, the degradation rate subsequently declined, owing to the shielding effect exerted by the photocatalyst

particles. The decrease in photocatalytic degradation efficiency can be attributed to the reduction in the generation of electron–pairs [59]. The photocatalyst was used repeatedly to determine how stable it was after being manufactured [60].

#### 3.8.1 Effect of the pH on Rh B

It is important to note that the pH level in a photocatalytic reactor has a significant effect on the surface-charge

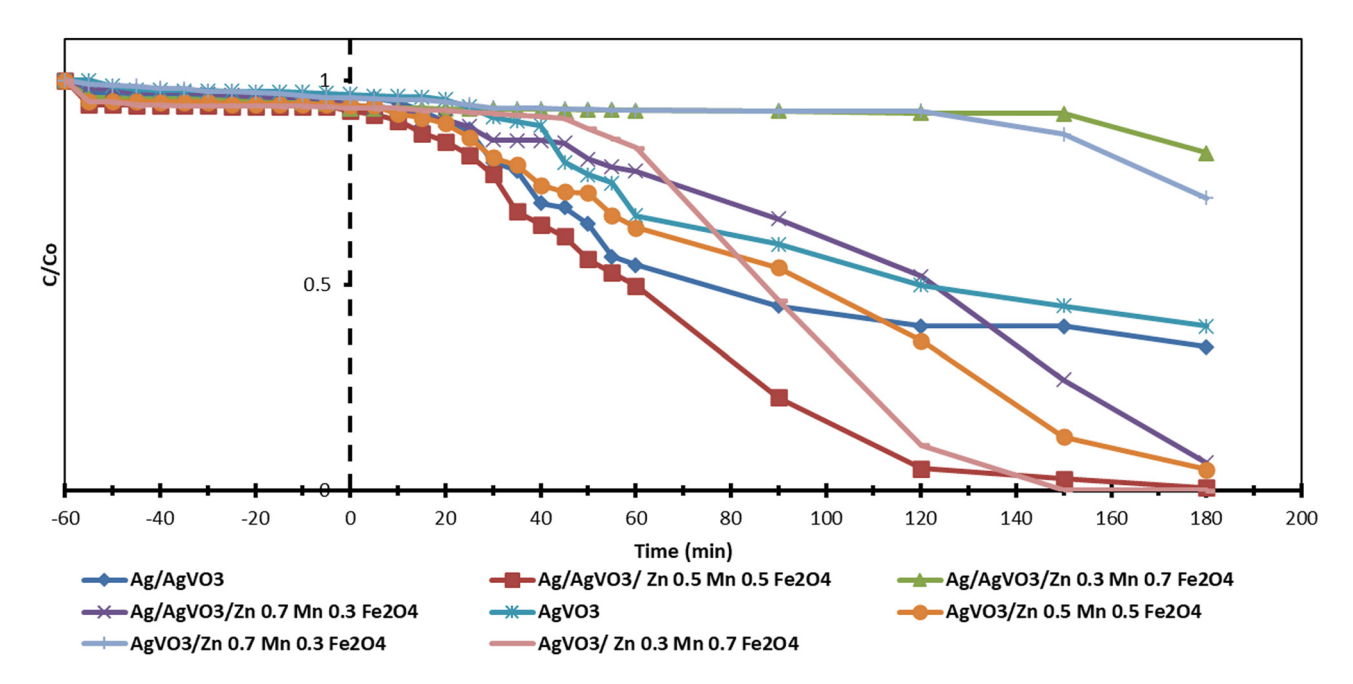


Figure 18: Plot for the photocatalytic degradation of Rh B dye for  $Zn_{0.5}Mn_{0.5}Fe_2O_4/Ag/AgVO_3$  versus time.

properties of the photocatalyst and the make-up of ionic species. The ionic composition also has an impact on the efficiency of dye photodegradation [61,62].

Rh B photodegradation without NPs, with the apparent rate constant varying as a function of starting pH (Figure 20). Rh B was present at a concentration of 1 g/L, hydrogen peroxide was present at a concentration of 120 mM, and the

irradiation period was 180 min. Sets of experiments were set up to investigate how different pH values affected the rate at which Rh B degraded when exposed to visible light. In the first set, pH was changed from 2 to 12, but Rh B and  $\rm H_2O_2$  concentrations were held steady. Surprisingly, it was shown that neutral and acidic pHs were more successful in this system with regard to Rh B photodegradation (Figure 20).

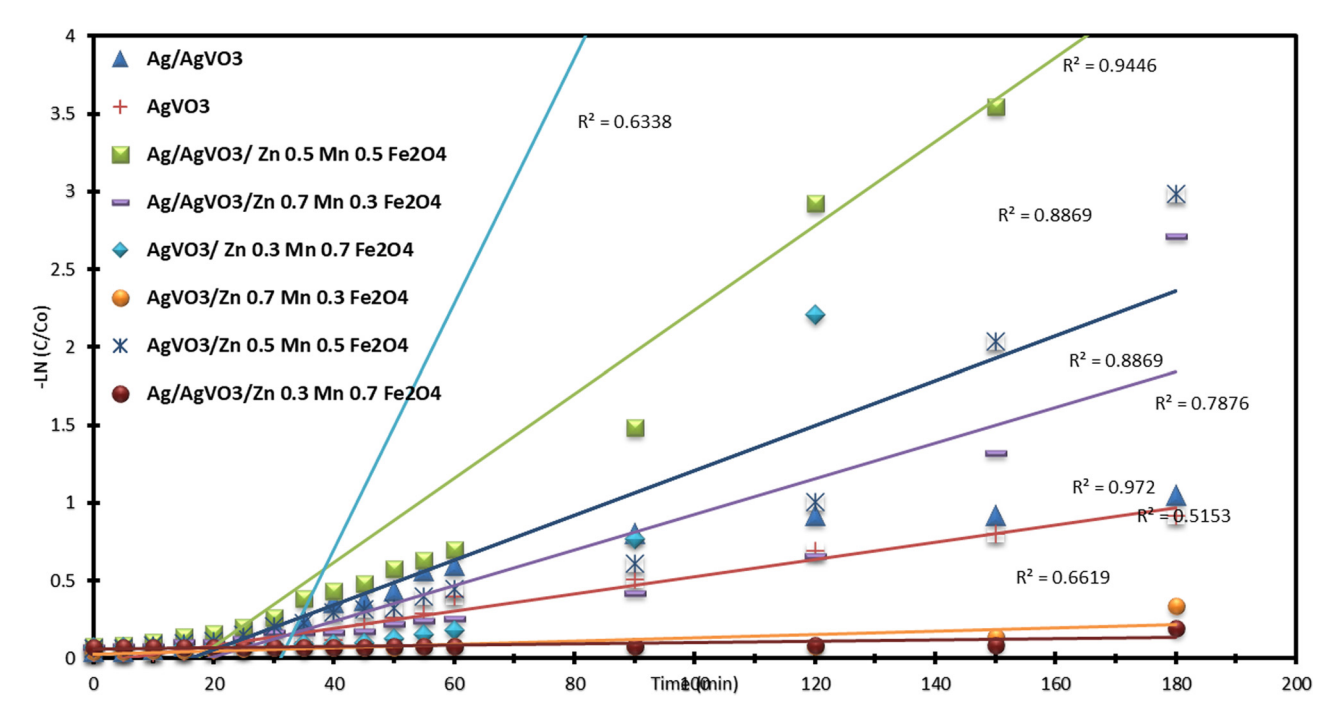


Figure 19: Kinetic model for the supported Zn<sub>0.5</sub>Mn<sub>0.5</sub>Fe<sub>2</sub>O<sub>4</sub>/Ag/AgVO<sub>3</sub> nanocomposites.

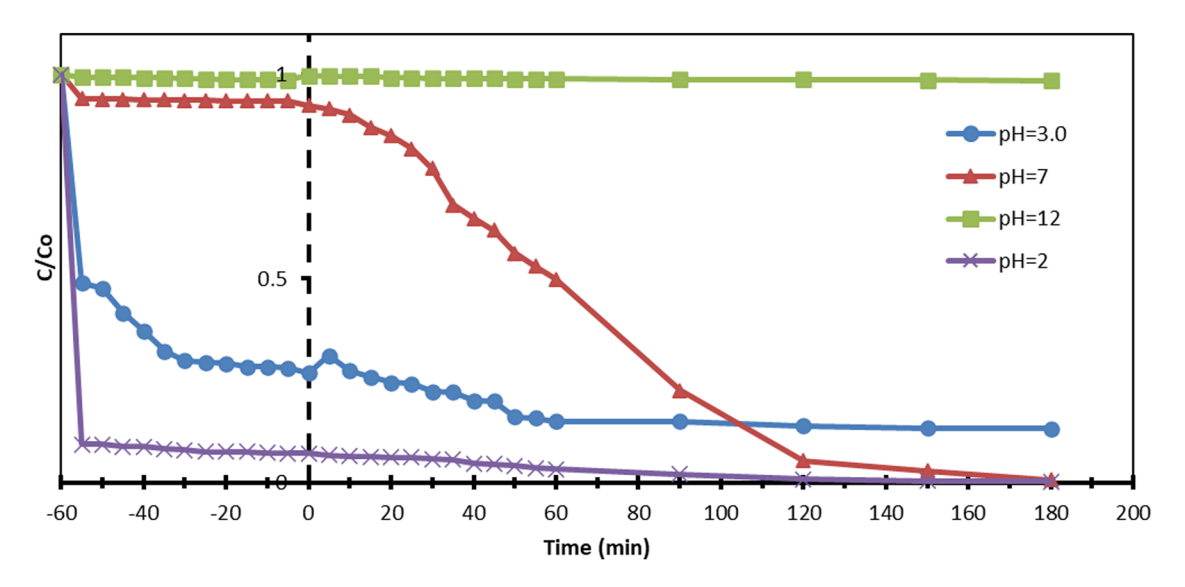


Figure 20: Effect of acidity and alkalinity of solution on the photocatalytic degradation activity of Rh B dye of Zn<sub>0.5</sub>Mn<sub>0.5</sub>Fe<sub>2</sub>O<sub>4</sub>/Ag/AgVO<sub>3</sub>.

Degradation of Rh B was found to be dramatically sped up at lower pH values (p $K_a = 2$ ) by significantly increasing the fraction of the more reactive deprotonated form of hydrogen peroxide (HO<sub>2</sub>) [12].

A near-neutral or acidic pH may be most favorable for this kind of interaction, as shown by the influence of pH in the presence of  $Zn_{0.5}Mn_{0.5}Fe_2O_4/Ag/AgVO_3$  (Figure 20). The apparent rate constant was highest at a pH of 2, but additional increases in pH slowed the reaction slightly. The partially hydroxylated forms of the metal ions were also detected at the local maximum of roughly pH = 2, as shown in Figure 21.

Rh B in the reaction mixture can have its charge state changed by the pH. Furthermore, Rh B aggregates are

generated at high pH values because of the overabundance of OH– ions, which compete with COO– to bind with metal ferrite [30,63]. Furthermore, under basic conditions, the Rh B is repelled by the solid catalyst's negatively charged surface, which is composed of ionic COO– groups [64].

As a result, photocatalyst surface degradation efficiency is reduced [4,44]. However, similar to the reaction without NPs, the rate was significantly increased at pH values below 3.

The pH value determines the surface-charge characteristics of the catalyst and the size of aggregates it forms, which in turn affects the rate of degradation of various organic chemical contaminants [12,16,22,65]. Thus, it was tested the degradation of Rh B dye at 2, 3, 7, and 11 pH levels to

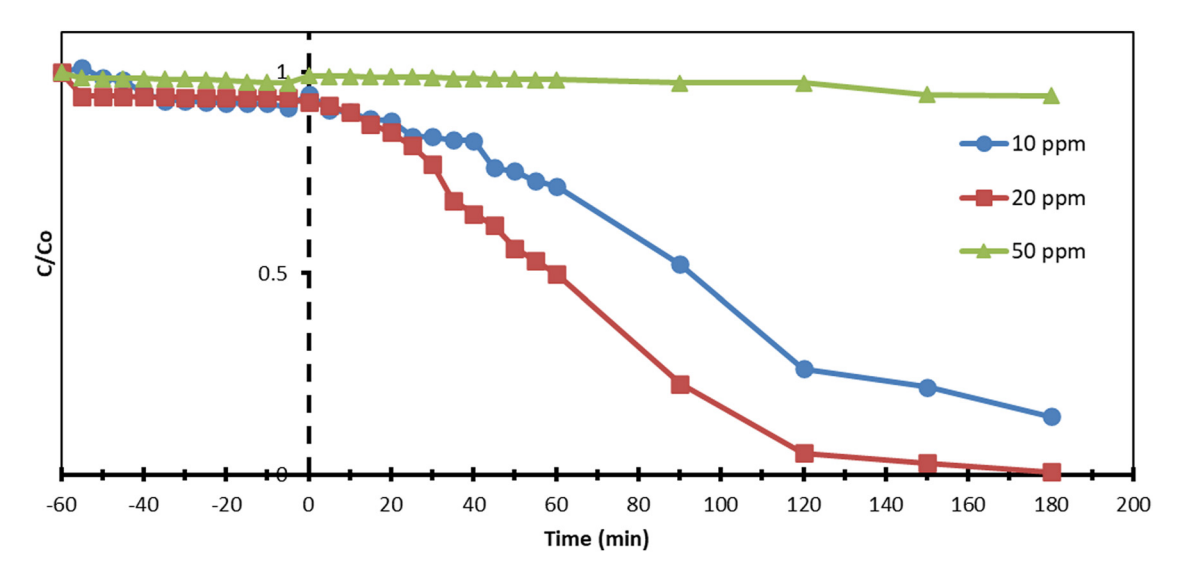


Figure 21: Impact of varying concentrations of (Rh B) dye on the photocatalytic degradation efficiency for Zn<sub>0.5</sub>Mn<sub>0.5</sub>Fe<sub>2</sub>O<sub>4</sub>/Ag/Ag/AgVO<sub>3</sub>.

investigate how pH affects the process. The results show the degradation percentage of Rh B dye was 99.9% at pH 2, 95.1% at pH 3, 93.5% at pH 7, and 11.3% at pH 12.

The rate of degradation was found to decrease as the pH rise. When reactions take place on the surface of a semiconductor, the amphoteric behavior of the metal oxide might affect the catalyst's surface-charge (pzc) characteristics [16,59]. Consequently, a greater number of negatively charged anions Rh B are visible on the surface of supported catalyst at low pH values, as their positively charged nature is reduced at pH values lower than the pH $_{\rm pzc}$  value. This effect is mainly caused by the fact that the electrostatic interaction between the Rh B dye molecule and the supported catalyst increases at low pH values, leading to accelerated dye degradation. The results agreed with those of a previous study in which the core/shell  $\rm Zn_{0.5}Mn_{0.5}Fe_2O_4@Ag-AgVO_3$  nanocomposite expressed higher performance of Rh B degradation at low pH (it is equal to 2).

## 3.8.2 Effect of concentration pollutant on the photodegradation efficiency

Figure 21 shows the influence of both contaminant concentration and reaction rate. The values of the turnover numbers did not vary with the concentration of the contaminants below a threshold of 7.5 ppm. The sales volume dropped as increased levels of contamination. There was a correlation between the variation in contaminant concentration and the quantum yield values [66].

There was no correlation found between contaminant concentration and the rate of photodegradation, and in certain situations, the rate decreased with higher initial concentration [3]. Several hypotheses are put forward; however, all of these theories revolve around the process of adsorption, specifically the binding of contaminant molecules onto the surface of a solid material, as described by the Langmuir–Hinshelwood model [67]. The molecules of the contaminants themselves may compete with oxygen, or the adsorption intermediates to slow down the breakdown process at greater concentrations [3,18,68].

With a high concentration of pollutants, the catalyst's active sites might be filled with adsorbed reactant molecules, resulting in a slowdown in degradation (zero-order kinetics). The process of target pollutant adsorption on photocatalyst surface increases with increasing concentration, as demonstrated in multiple experiments. Hence, necessary reactive species ('OH and 'O<sub>2</sub>) for pollutant breakdown are also required in greater quantities.

As long as the light intensity, catalyst amount, and irradiation duration are consistent, the creation of 'OH and 'O<sub>2</sub> on the catalyst surface will not change [69]. This means

that increased concentrations of pollutants will not be degraded by the currently available OH radicals. Therefore, when the concentration increases, the rate of pollutant breakdown reduces. The production of intermediates, which might adsorb on the catalyst surface, can also result from a higher substrate concentration. When the produced intermediates take their time to diffuse from the catalyst surface, it can deactivate the photocatalyst's active sites and slow down the degradation rate. When the concentration is low, however, the apparent firstorder kinetics states that the substrate concentration is directly proportional to the degradation rate and that the number of catalytic sites is not a limiting factor [19]. Several studies used the "Langmuir-Hinshelwood" (L-H) kinetics model to effectively characterize how the rates of photocatalytic degradation depend on the concentrations of different organic in order to explain how the reaction rate varies with different starting solute concentrations [66].

#### 3.8.3 Effect of H<sub>2</sub>O<sub>2</sub> on Rh B

At first, from Figure 22, it was observed that  $H_2O_2$  affected the photodegradation of Rh B when no nanocomposites were present.  $H_2O_2$  levels were raised from 120 up to 240 mM bringing the  $H_2O_2$  concentration up to 360 mM sped up the reaction. The apparent rate constant, however, was shown to decline slightly beyond this number. At 120 mM of hydrogen peroxide, the removal efficiency was high (99%). However, the increasing concentration of  $H_2O_2$  leads to a lower degradation rate (80%) and (20%).

In the second set of experiments, it was examined what would happen if the  $\rm H_2O_2$  concentration is increased in a heterogeneous photocatalytic process. Bringing the  $\rm H_2O_2$  concentration up to 360 mM significantly sped up the reaction, but it showed a lower degradation rate of Rh B. In addition, comparable results have been published in the literature [70,71], indicating that increasing the  $\rm H_2O_2$  concentration did not significantly increase the reaction rate. The extra  $\rm H_2O_2$  may function as a scavenger for 'OH, converting it to the less reactive  $\rm HO^{'2}$  species [4,71,72].

An increase in the concentration of hydroxyl radicals was one of the mechanisms that were thought to explain why adding hydrogen peroxide improved reaction rates and revealed the presence of an optimal outcome. High concentration of hydrogen peroxide has the potential to adsorb organic pollutants alongside it at catalytic active sites in which leading to low degradation rate. The optimum condition showed that at 120 mM of hydrogen peroxide, the degradation efficiency was 99.9% for Rh B. The results were agreed with Jasim *et al.* [4] in which stated that at low concentration of  $H_2O_2$ , the rate degradation of Rh B was

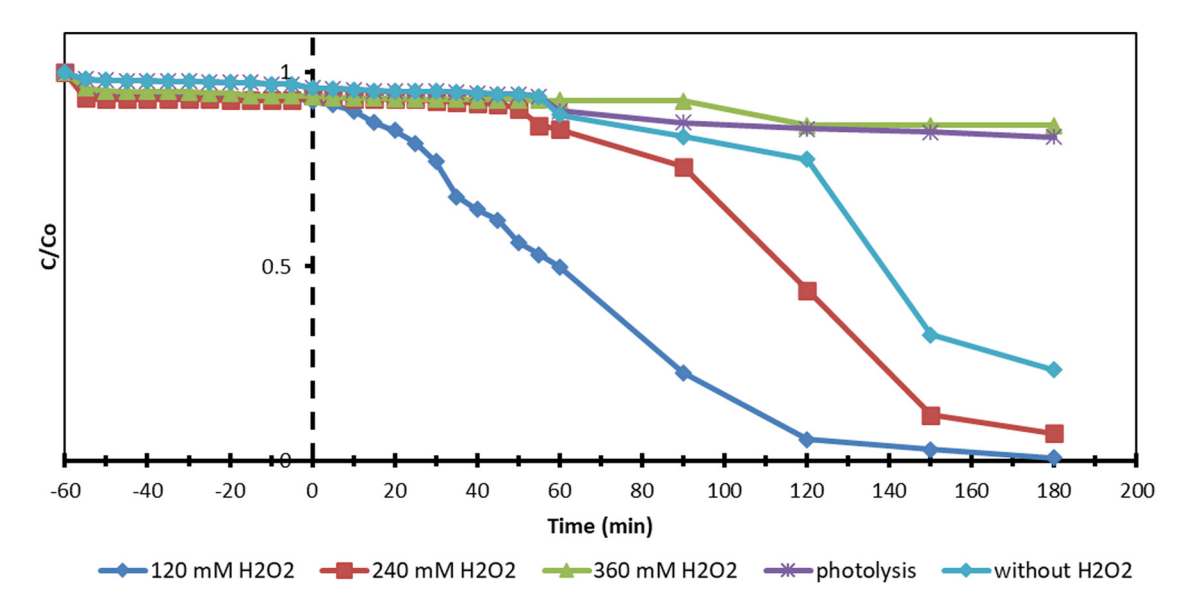


Figure 22: Effect of H<sub>2</sub>O<sub>2</sub> addition on the removal efficiency of Rh B dye for Zn<sub>0.5</sub>Mn<sub>0.5</sub>Fe<sub>2</sub>O<sub>4</sub>/Ag/AgVO<sub>3</sub>,.

achieved using the core/shell  $\rm Zn_{0.5}Mn_{0.5}Fe_2O_4$  @Ag–AgVO $_3$  catalyst.

It was found that the catalysts' active sites – specifically, oxygen for hydrogen peroxide – had stronger contacts. The cationic reactive Rh B dye had its degradation rates reduced for a number of reasons, one of which was competitive adsorption by hydrogen peroxide at large concentrations [73].

Thus, adding hydrogen peroxide will have two beneficial effects: (a) more available holes for oxidation, leading to better hydroxyl radical generation, and (b) more hydroxyl radicals formed directly as a result of the conduction band (CB) electron reducing  $H_2O_2$ . Thus, organic pollutants will be

degraded more quickly in environments where hydroxyl radical generation is more rapid.

#### 3.8.4 Effect of the dose of catalyst on the Rh B

The elimination efficiency exhibited a significant enhancement when the dosage of the catalyst was augmented from 1 to 1.5 mg/L. The increased availability of active sites in heterogeneous photocatalytic processes is responsible for this phenomenon [72]. Higher concentrations of supported  $\rm Zn_{0.5}Mn_{0.5}Fe_2O_4/Ag/AgVO_3$  can enhance turbidity in the reaction system, reducing light absorption, which may

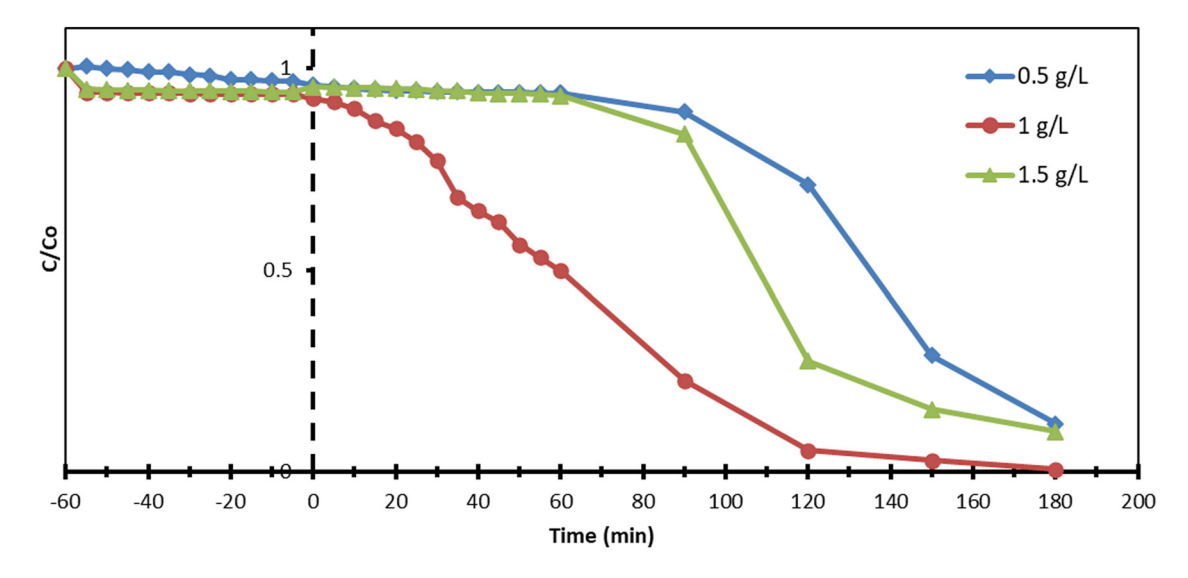


Figure 23: Influence of catalyst dosage on the removal efficiency of Rh B dye for supported Zn<sub>0.5</sub>Mn<sub>0.5</sub>Fe<sub>2</sub>O<sub>4</sub>/Ag/Ag/AgVO<sub>3</sub>.

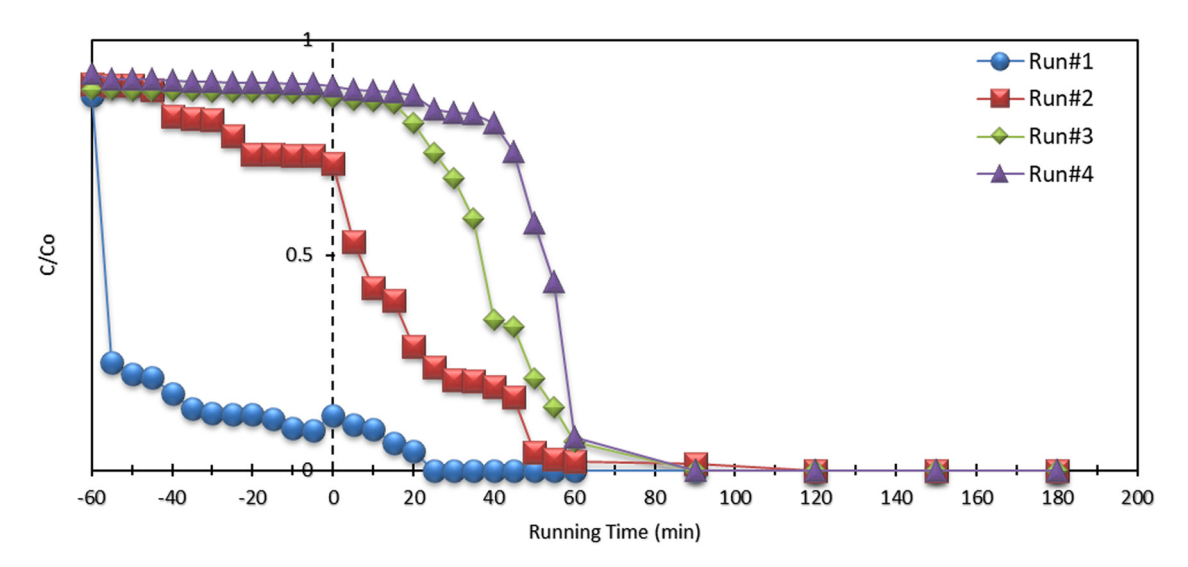


Figure 24: Reusing studies of Zn<sub>0.5</sub>Mn<sub>0.5</sub>Fe<sub>2</sub>O<sub>4</sub>/Ag/AgVO<sub>3</sub> nanocomposites under the visible light irradation system.

explain why increasing the dosage of  $Zn_{0.5}Mn_{0.5}Fe_2O_4/Ag/Ag/O_3$  over 50 mg/L resulted in a modest decrease in the removal efficiency [4]. Therefore, a concentration of 50 mg/L was used in the subsequent photocatalytic experiments, as revealed in Figure 23.

With an increasing dose of catalyst in 25 ppm Rh B dye, the photodegradation efficiency was discovered to decrease sharply. The supported nanocomposites synthesized by the percentage of (10% W of Zn<sub>X</sub>Mn<sub>(1-X)</sub>Fe<sub>2</sub>O<sub>4</sub> and 90% W of Ag@AgVO<sub>3</sub>) showed less rate of degradation when the dose of catalyst increased (81%) at 1.5 g/L. Because supported nanocomposite has a stronger UV absorption and can break the Rh B molecule more efficiently than others at even low catalyst dose. In addition, the release of free oxidative radicals (such as hydroxyl radicals 'OH) into the water solution by catalysts has a greater ability to break down Rh B. The supported nanocomposite was able to reach 99.9% degradation after 3h of degradation. In a batch reactor, the following decontamination method made use of just 1 g/L of the catalysts in order to preserve the water's physical and chemical conditions and the performance of degradation was achieved at 0.1 mg of catalysts.

## 4 Reusing efficiency

The optimized  $Zn_{0.5}Mn_{0.5}Fe_2O_4/Ag/AgVO_3$  nanocomposite was used in five separate photodegradation runs, all of which yielded results that showed the photocatalyst could be used after being prepared (Figure 24). The degradation performance barely dips after three cycles. Consequently, the results demonstrated that the optimized  $Zn_{0.5}Mn_{0.5}Fe_2O_4/Ag/AgVO_3$ 

demonstrated the photostability, and the recyclable nature of nanocomposite photocatalysts were exceptionally high.

In Figure 25, the recyclabity and stability studies are demonstrated for the supported  $Zn_{0.5}Mn_{0.5}Fe_2O_4/Ag/AgVO_3$  under the VLI system. The first run was equal to 99.999%, the second run was equal to 98.49%, the third run was 93.569%, and the fourth run was 92.5%, which reduced. The first run was the best one in the removal efficiency. Figure 26 represents the kinetic model for the photocatalytic degradation for the supported  $Zn_{0.5}Mn_{0.5}Fe_2O_4/Ag/AgVO_3$ .

## 5 Scavenger studies

The photodegradation mechanism can be better understood by looking into the parts played by several active

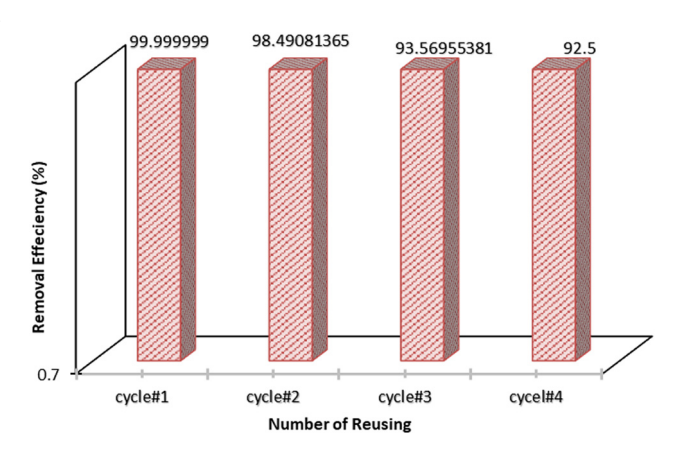


**Figure 25:** Recyclability and stability studies of  $Zn_{0.5}Mn_{0.5}Fe_2O_4/Ag/Ag/O_3$  nanocomposites under the VLI system.

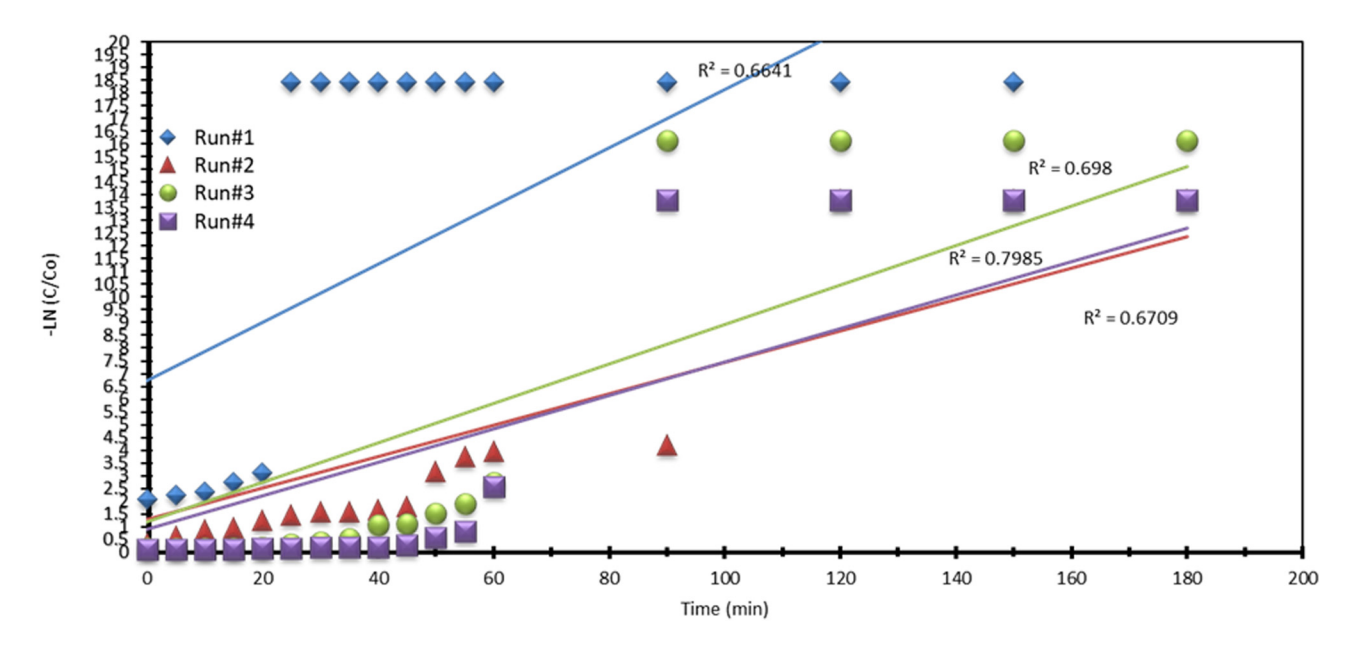


Figure 26: Kinetic modeling for the reusing studies for the nanocomposite Zn<sub>0.5</sub>Mn<sub>0.5</sub>Fe<sub>2</sub>O<sub>4</sub>/Ag/AgVO<sub>3</sub>.

species (including "h<sup>+</sup>, e<sup>-</sup>, H<sub>2</sub>O<sub>2</sub>, 'O<sub>2</sub>, and 'OH") in the degradation of the Rh B dye. According to Figure 26, a number of scavenging tests were conducted with Zn<sub>0.5</sub>Mn<sub>0.5</sub>Fe<sub>2</sub>O<sub>4</sub>/Ag/ AgVO<sub>3</sub> present during the course of this investigation. In contrast, sodium oxalate, potassium dichromate, sodium-EDTA, P-benzoquinone, and isopropanol, respectively, were able to capture the photoactive species of h<sup>+</sup>, e, H<sub>2</sub>O<sub>2</sub>, ˙O<sub>2</sub><sup>-</sup>, and OH. The effectiveness of photocatalytic degradation was as follows: 7.4% when sodium oxalate, potassium dichromate, sodium-EDTA, P-benzoquinone, and isopropanol were each

**DE GRUYTER** 

added at concentrations of 0.5 mmol/L: 50, 0.65, 78, and 1.11% correspondingly.

Experiments with photocatalysis were performed with the assistance of various scavengers, and the results are depicted in Figure 27. This was carried out to identify the relative importance of the several reactive substances (h<sup>+</sup>, 'OH, and others) in the photocatalytic destruction of Rh B. The hydroxyl (h+) and hydroxyl (OH) radicals appear to play a significant role in the oxidation of Rh B. P-benzoquinone scavenger was the most efficient one in the degradation process.

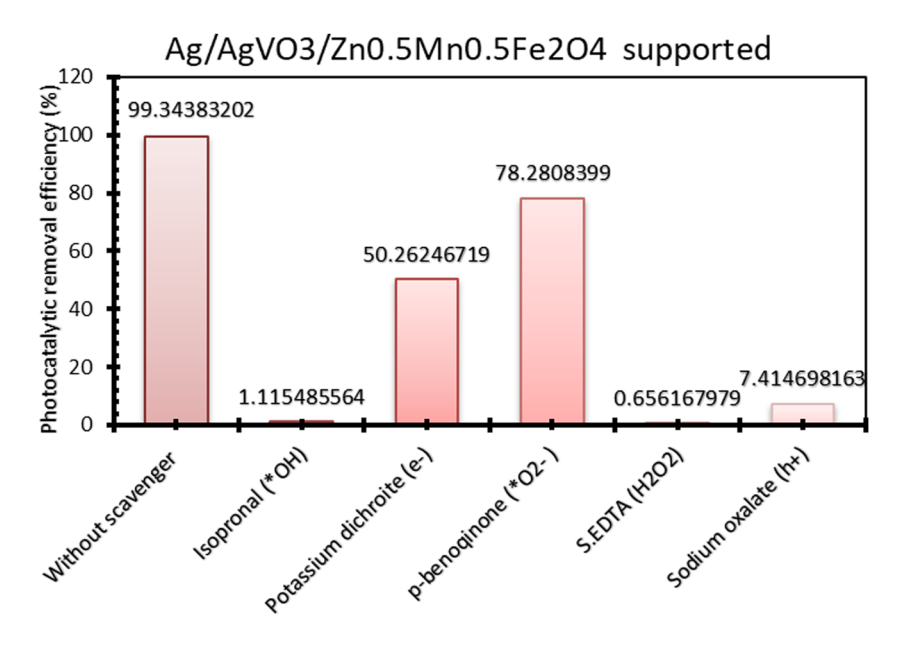


Figure 27: Different scavenger types and their effect on the degradation efficiency.

Table 3: Valence band (VB) and CB potentials of  $AgVO_3$  and  $Zn_{0.5}Mn_{0.5}Fe_2O_4$ 

Semiconductor	E <sub>VB</sub> (eV)	E <sub>CB</sub> (eV)	
AgVO <sub>3</sub>	2.41	0.660	
$Zn_{0.5}Mn_{0.5}Fe_2O_4$	2.036	0.536	

# 6 Possible photocatalytic mechanism

The photocatalytic activity is fundamentally supported by the capacity to generate, transfer, and subsequently disassociate photo-generated electron–hole pairs [74]. The following empirical formulas were used to determine the band locations of  $Ag/AgVO_3$  and  $Zn_{0.5}Mn_{0.5}Fe_2O_4$  (Table 3).

A previous study used the Butler-Ganley equation:

$$E_{\rm VB} = X - E_{\rm e} + 0.5 E_{\rm g}.$$
 (3)

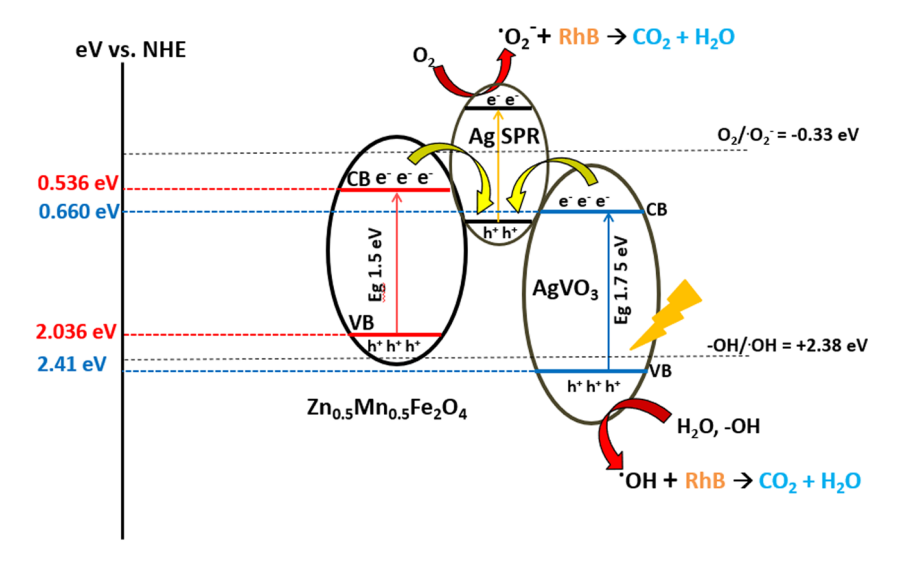
To determine the valence and CB potentials of the asprepared photocatalysts,

$$E_{\rm VB} - E_{\rm g} = E_{\rm CB}. \tag{4}$$

In this case,  $E_{\rm VB}$  stands for the potential of the VB edge,  $E_{\rm CB}$  for the potential of the CB edge, X for the semi-conductor's electronegativity (found by taking the geometric mean of the electronegativity values of its constituent atoms),  $E_{\rm e}$  for the energy of free electrons on the hydrogen scale (about 4.5 eV), and  $E_{\rm g}$  for the semiconductor's bandgap energy.

The computed edge potentials for the Ag/AgVO<sub>3</sub> system are determined to be 2.41 eV for the VB and 0.660 eV for the CB. In addition, it is seen that Zn<sub>0.5</sub>Mn<sub>0.5</sub>Fe<sub>2</sub>O<sub>4</sub> exhibits a VB edge potential of 2.036 eV and a CB edge potential of 0.536 eV. This observation is consistent with prior reports where each of these scavengers, namely h+, OH, and  $(O_2^-)$ , was employed to mitigate active sites, facilitating a more comprehensive investigation of the photocatalytic mechanism. The figure in this study demonstrates that the degradation of Rh B was significantly impeded when EDTA was present as a scavenger, in contrast to the absence of any scavenger. This observation suggests that active holes (h<sup>+</sup>) play a crucial role as the primary active component. The results suggest that the degradation rate of the photocatalysis process was reduced, showing the participation of both hydroxyl radicals ('OH) and superoxide radicals (' $O_2$ ') in the photocatalytic processes.

Based on the aforementioned calculations, it can be inferred that  $AgVO_3$  and  $Zn_{0.5}Mn_{0.5}Fe_2O_4$  exhibit the ability to produce photoexcited electron hole pairs (e<sup>-</sup>/h<sup>+</sup>) when exposed to visible light. This phenomenon is visually represented in Figure 28, illustrating the proposed mechanism for the process of photocatalytic degradation facilitated by the nanocomposite photocatalyst. The aforementioned experimental data has been utilized to propose a method for the process of photocatalytic degradation of Rh B dye using the  $Zn_{0.5}Mn_{0.5}Fe_2O_4/Ag/AgVO_3$  composite under visible light conditions (as depicted in Figure 29). When  $Ag/AgVO_3$  is subjected to visible light, electrons (e<sup>-</sup>) have the ability to undergo excitation from the VB to the CB. This process,



Z-scheme Zn<sub>0.5</sub>Mn<sub>0.5</sub>Fe<sub>2</sub>O<sub>4</sub>/Ag/AgVO<sub>3</sub> plasmonic heterojunction

 $\textbf{Figure 28:} \ \ \textbf{Schematic representation of } \ Zn_{0.5} Fe_2O_4/Ag/AgVO_3 \ \ \textbf{nanocomposite photocatalyst toward the degradation of Rh B under VLI.}$ 

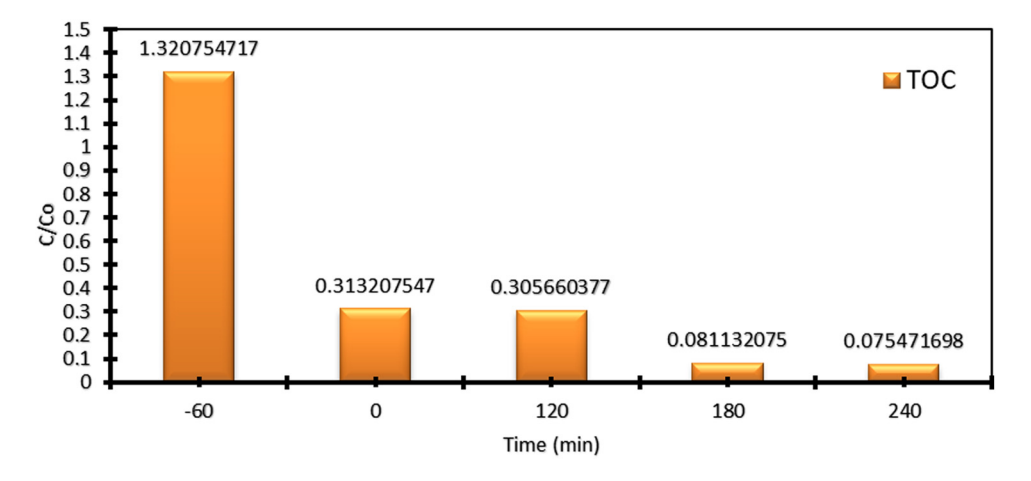


Figure 29: COD removal efficiency of Zn<sub>0.5</sub>Mn<sub>0.5</sub>Fe<sub>2</sub>O<sub>4</sub>/Ag/AgVO<sub>3</sub> against Rh B dye.

however, results in the creation of a vacancy or "hole" within the VB. Nevertheless, the optical absorption of  $Zn_{0.5}Mn_{0.5}Fe_2O_4$  is limited due to its substantial band gap energy. To generate electrons, the surface of metal ferrite was used as a substrate for the adsorption of Rh B molecules. Subsequently, these Rh B molecules were subjected to visible light, thereby inducing a stimulation that facilitated the injection of electrons into the CB of  $Zn_{0.5}Mn_{0.5}Fe_2O_4$ . As a consequence, the process led to the effective dissociation of electron–hole pairs. Subsequently, within the supported nanocomposite, oxygen has the capability to confine electrons, resulting in the formation of  $(O_2)$ , reactive species. These reactive species, in turn, have the capacity to produce 'OH. The molecules of Rh B dye exhibit vulnerability to direct oxidation by reactive species such as  $(O_2)$ , 'OH, and h<sup>+</sup>.

In the context of VLI, the migration of photoexcited electrons from the CB of  $AgVO_3$  to the CB of  $Zn_{0.5}Mn_{0.5}Fe_2O_4$  occurs within a nanocomposite photocatalyst. This phenomenon is illustrated in the schematic representation of the  $Zn_{0.5}Mn_{0.5}Fe_2O_4$ 

 $Ag/AgVO_3$  nanocomposite photocatalyst, which is utilized for the degradation of Rh B. Concurrently, the holes created by light (h<sup>+</sup>) are transported from the VB of  $AgVO_3$  to the VB of  $Zn_{0.5}Mn_{0.5}Fe_2O_4/Ag/AgVO_3$ , thereby improving the efficiency of separating charge carriers [54].

# 7 TOC and chemical oxygen demand

Figure 29 depicts the shift that takes place in TOC during photocatalytic degradation of Rh B using supported  $Zn_{0.5}Mn_{0.5}Fe_2O_4/Ag/AgVO_3$  as the catalyst in the presence of VL. The TOC tests demonstrated an absence of organic carbon was produced when the Rh B solution, which included either  $Zn_{0.5}Mn_{0.5}Fe_2O_4/Ag/AgVO_3$  was subjected

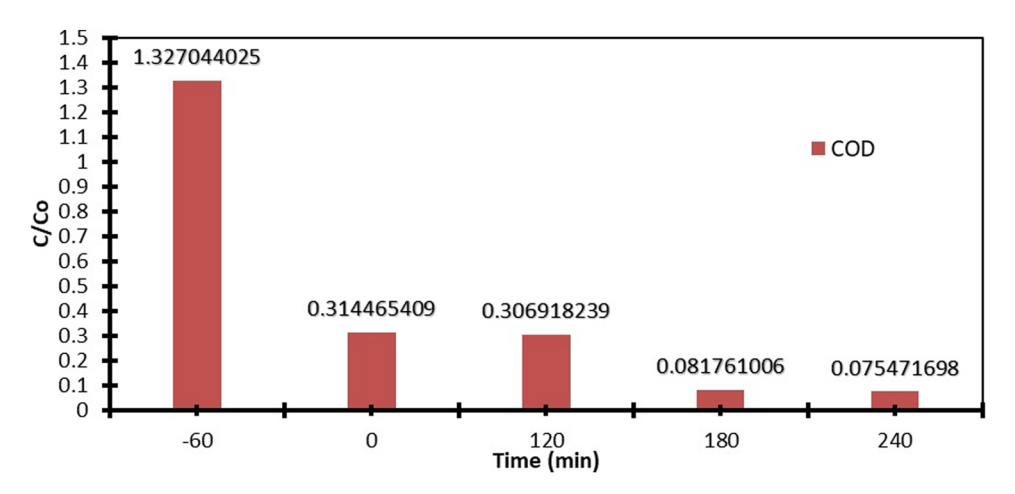


Figure 30: COD removal efficiency of Zn<sub>0.5</sub>Mn<sub>0.5</sub>Fe<sub>2</sub>O<sub>4</sub>/Ag/AgVO<sub>3</sub> against Rh B dye.

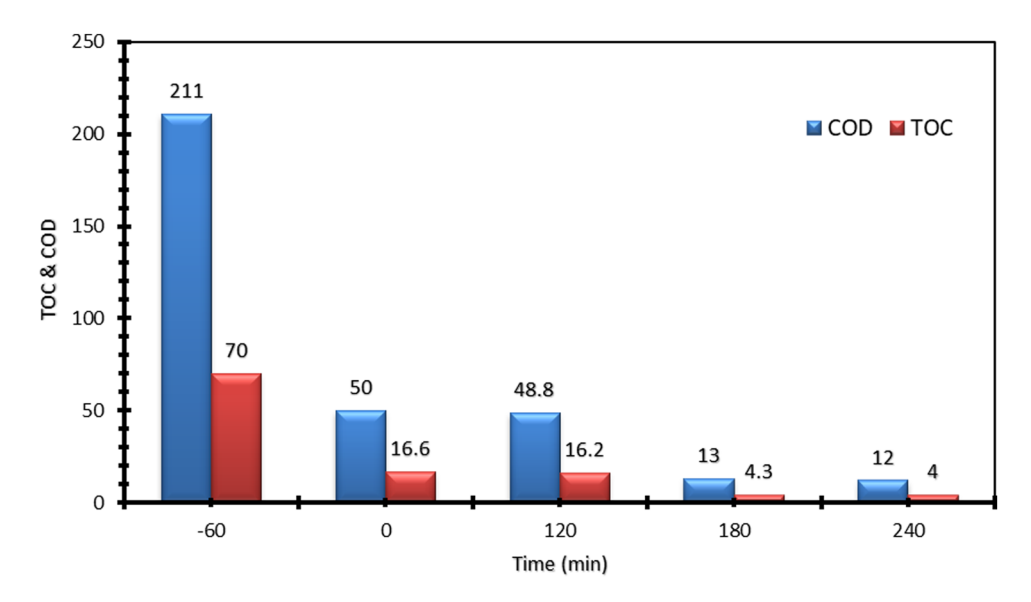
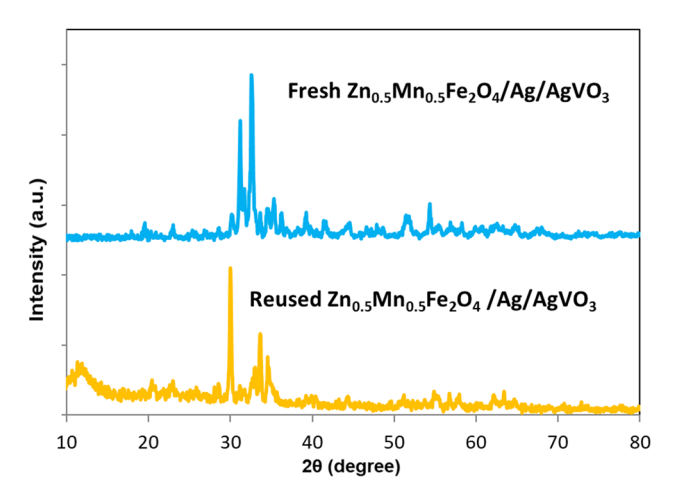


Figure 31: TOC removal efficiency and COD of Zn<sub>0.5</sub>Mn<sub>0.5</sub>Fe<sub>2</sub>O<sub>4</sub>/Ag/AgVO<sub>3</sub> against Rh B dye.

to the irradiation of visible light. Following an exposure period of 180 min to VL, the results showed that a decrease in TOC of 70, 16.6, or 4.3% was obtained when the photocatalyst utilized. As a consequence of this, the total mineralization of Rh B was expressed following VLI for 180 min using  $\rm Zn_{0.5}Mn_{0.5}Fe_2O_4/Ag/AgVO_3$  as the catalyst. This was due to the elimination of 100% of the TOC.

The results of the studies that were carried out demonstrated that photocatalysis of Rh B is an effective method for COD degradation. The findings also demonstrated that the method is effective when a catalyst is added to the mixture.

According to the findings, COD in synthetic wastewater can be reduced by the use of photodegradation; however,



**Figure 32:** XRD patterns before and after reusing of the supported nanocomposites.

for the procedure to be effective, more processing time and a catalyst are required.

Based on an analysis of the data shown in Figures 29–31, it can be inferred that pH exerts a notable influence on the reduction of COD. When the COD was changed to have a pH of 2, the results revealed a reduction in COD of 26%, while the experiment was carried out under the same conditions. In order to avoid any kind of contamination, the research suggests that the process should be carried out for more than 2 h.

In addition, the expected 50% reduction in COD might have been attained if the pH was altered to be more acidic (<2), and this was determined by examining the results that were obtained. If the procedure was carried out in both batch and continuous modes, the result could demonstrate a variation in either of these two modes. The process could only be carried out in batch form because there was insufficient time.

The above experimental results will be used to suggest a reaction mechanism for the breakdown of dyes in visible light using a composite photocatalyst composed of supported  $\rm Zn_{0.5}Mn_{0.5}Fe_2O_4/Ag/AgVO_3$ . Since  $\rm Zn_{0.5}Mn_{0.5}Fe_2O_4$  has a lower conduction energy level, the photo-generated electrons that excite it will jump to the CB of AgVO<sub>3</sub> instead. Silver, which is a very good conductor of electricity and has a lot of electronic storage space, helps keep AgVO<sub>3</sub> from breaking down. This is achieved by the absorption of surplus photo-generated electrons within the CB of the complex [75].

According to earlier research, photo-generated electrons can effectively move from  $Zn_{0.5}Mn_{0.5}Fe_2O_4$  to  $AgVO_3$  and then to Ag, or they can only move from  $Zn_{0.5}Mn_{0.5}Fe_2O_4$  to  $AgVO_3$ .  $Ag/AgVO_3$  can be used as a medium to help photo-

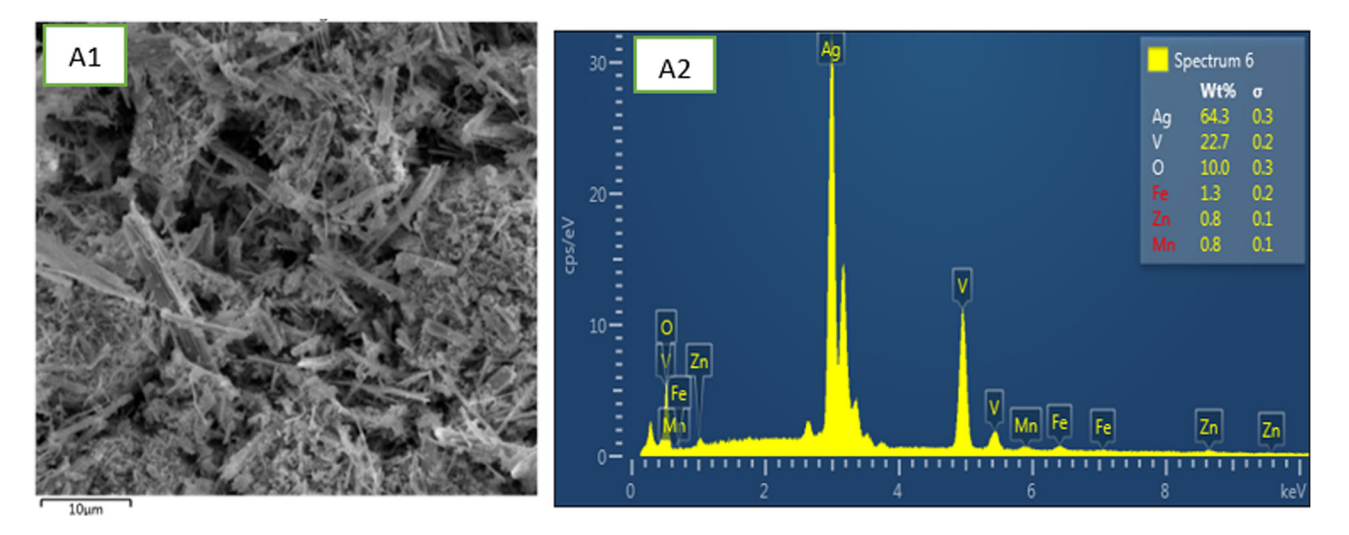


Figure 33: EDS analyses for the supported nanocomposites.

generated electrons move around in the Zn<sub>0.5</sub>Mn<sub>0.5</sub>Fe<sub>2</sub>O<sub>4</sub>/Ag/ AgVO<sub>3</sub> system. This will lower the chance of photo-generated electrons and holes recombining and improve the separation of photo-generated carriers. Photo-induced holes on Ag nanoparticles and photo-generated holes from AgVO<sub>3</sub> can break down Rh B dye into its own degradants. The photochemical activity of silver nanoparticles creates electrons that react with oxygen in the air. These electrons start the process of making the highly reactive oxygen radical  $O^2$ . This radical subsequently gives rise to the hydroxyl radical OH, leading to the degradation of the dye [69]. The use of silver in the prevention of the reduction of AgVO<sub>3</sub> is attributed to its exceptional conductivity and significant electronic storage capacity. This is achieved by the absorption of surplus photo-generated electrons in the CB of the compound. Finally, it was noted that the hydroxyl radical (OH) and other ROS such as O<sup>2</sup> and photo-induced holes (PiH) have the potential to degrade Rh B [54,67,76,77].

The supported  $Zn_{0.5}Mn_{0.5}Fe_2O_4/Ag/AgVO_3$  is so effective at catalyzing the breakdown of dye when exposed to visible light. Visible light can be absorbed more efficiently in large quantities when Ag nanoparticles are present. Dyes are more effectively adsorbed onto the catalyst surface when metal ferrite is also present. The separation of photo-generated carriers is improved, and the photocatalytic performance of samples is elevated with the help of AgVO<sub>3</sub> and  $Zn_{0.5}Mn_{0.5}Fe_2O_4$ .

Many researchers in recent years have used various photocatalysts to investigate dye degradation, but their results have not been as promising as those presented here. There are additional studies that use silver metavanadate nanocomposite for degradation [74]. This article contributes to the body of knowledge through the investigation

of the supported Zn<sub>0.5</sub>Mn<sub>0.5</sub>Fe<sub>2</sub>O<sub>4</sub>/Ag/AgVO<sub>3</sub> in which contributed as a more effective photocatalyst for dye degradation.

## 8 Reusing characterizations for Zn<sub>0.5</sub>Mn<sub>0.5</sub>Fe<sub>2</sub>O<sub>4</sub>/Ag/AgVO<sub>3</sub>

Catalysts' stability is crucial to their usefulness in the real world. As a result, the  $\rm Zn_{0.5}Mn_{0.5}Fe_2O_4/Ag/AgVO_3$  composite photocatalyst was employed to degrade Rh B for a total of five times in the identical conditions. The results display that the removal efficiency of the  $\rm Zn_{0.5}Mn_{0.5}Fe_2O_4/Ag/AgVO_3$  composite photocatalyst was virtually unaffected after five cycles, attesting to its excellent recyclability. It was compared the XRD pattern of a used  $\rm Zn_{0.5}Mn_{0.5}Fe_2O_4/Ag/AgVO_3$  sample with a new one (Figure 34). As we can see, the concentration of Ag nanoparticles has increased from the fresh  $\rm Zn_{0.5}Mn_{0.5}Fe_2O_4/Ag/AgVO_3$  sample, as measured by the higher intensity of Ag in the used  $\rm Zn_{0.5}Mn_{0.5}Fe_2O_4/Ag/AgVO_3$  sample. This finding agrees with what Zhao et~al. reported that for silver ion's photosensitivity, Ag nanoparticles may be created by light irradiation [78,79].

#### 8.1 XRD

The XRD patterns of both recycled  $Zn_{0.5}Mn_{0.5}Fe_2O_4/Ag/Ag/Ag/O_3$  and freshly manufactured  $Zn_{0.5}Mn_{0.5}Fe_2O_4/Ag/Ag/O_3$  composites are displayed in Figure 32. There are two different diffraction peaks in pure that can be observed at around 27.6° and 30.1°, as well as 35.40°, and these peaks are indexed to the (002) and (100) crystal planes, respectively.

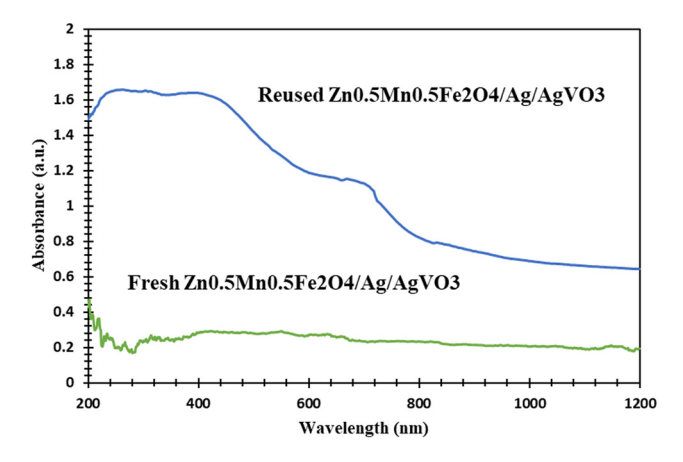


Figure 34: The DRS for nanocomposites before and after reusing.

After coupling with  $Zn_{0.5}Mn_{0.5}Fe_2O_4$ , the composites show diffraction peaks from both  $AgVO_3$  and  $Ag-AgVO_3$ , respectively. While this is going on, the  $Zn_{0.5}Mn_{0.5}Fe_2O_4$  diffraction peaks gradually weaken as the amount of  $Ag-AgVO_3$  increases. Furthermore, it has been observed that even Ag peaks can be detected, despite the diminutive size and low concentration of these particles within the composites. Following reuse, the XRD diffraction pattern was nearly comparable to that of the original, unrecycled form. These results revealed that the nanocomposites can be utilized for treatment after recycling since the XRD properties were comparable to those before reuse because they were similar to those before recycling.

#### 8.2 EDS

EDS tests are used to investigate the sample's chemical components, namely  $\rm Zn_{0.5}Mn_{0.5}Fe_2O_4/Ag/AgVO_3$ . The comprehensive survey spectrum presented in Figure 33 indicates beyond a reasonable doubt that the composite is composed of the element's manganese, zinc, iron, vanadium, and oxygen. The reference silver metavanadate is

the source of the peaks in the Ag spectra that are located at 37.7 CPS/eV. The EDS analysis showed that the chemical components of the  $\rm Zn_{0.5}Mn_{0.5}Fe_2O_4/Ag/AgVO_3$  nanocomposites were the same before and after they were reused. This indicates that the coupling of nanocomposites can be used for treatment even after the recycling process has been completed because there was no change in the chemical components of these nanocomposites. It is represented as the percentage weights for each element in Table 4, which shows that in order for the core/shell nanocomposites to be synthesized, 90% wt of  $\rm AgVO_3$  was employed, along with 10% wt of  $\rm Zn_{0.5}Mn_{0.5}Fe_2O_4$ . This was approved by the relevant authorities.

#### 8.3 DRS

Figure 34 illustrates the light absorption edge of the unadorned nanocomposites at around 460 nm in wavelength. The absorption of visible light in the range of 600–800 nm by the Ag/AgVO<sub>3</sub> sample can be attributed to the plasmon resonance of the silver present on the surface of the AgVO<sub>3</sub> crystal. The absorption edge of AgVO<sub>3</sub> is around 600 nm away from our current position. After coupling, the Zn<sub>0.5</sub>Mn<sub>0.5</sub>Fe<sub>2</sub>O<sub>4</sub>/Ag/AgVO<sub>3</sub> composites demonstrate increased absorption over the visible range, resulting in a redshift of the absorption edge.

This is in comparison with  $Zn_{0.5}Mn_{0.5}Fe_2O_4/Ag/AgVO_3$ . In addition, the intensity of the visible light absorbed increases proportionally with the amount of  $Ag/AgVO_3$  present. The absorbance intensities of the reused and new nanocomposites are shown in Figure 34, which demonstrates that they are comparable in the region of 800–1,000 nm. When  $Zn_{0.5}Mn_{0.5}Fe_2O_4/Ag/AgVO_3$  nanocomposites are mixed with metal ferrites, the visible absorption increases and the absorption edge shifts to the redder end of the spectrum. When there is a progressive increase in the amount of  $Ag/AgVO_3$ , absorption intensities also increase.

Table 4: Elements showed in the synthesis of core/shell nanocomposites

Element	Line type	Apparent concentration	k ratio	Wt%	Wt% Sigma	Atomic %	Standard label	Factory standard
0	K series	1.26	0.00423	10.05	0.29	36.50	SiO <sub>2</sub>	Yes
V	K series	5.16	0.05164	22.71	0.22	25.91	V	Yes
Mn	K series	0.19	0.00194	0.84	0.13	0.89	Mn	Yes
Fe	K series	0.31	0.00312	1 30	0.15	1.35	Fe	Yes
Zn	L series	0.08	0.00084	0.84	0.11	0.75	Zn	Yes
Ag	L series	14.54	0.14544	64.26	0.33	34.61	Ag	Yes
Total:				100.00		100.00	-	

#### 9 Conclusion

The fabrication of highly active  $Zn_{0.5}Mn_{0.5}Fe_2O_4/Ag/AgVO_3$  nanocomposite photocatalysts was made possible by a straightforward coprecipitation approach. In the course of this research, the optimized  $Zn_{0.5}Mn_{0.5}Fe_2O_4/Ag/AgVO_3$  nanocomposite photocatalyst demonstrated a significant enhancement in photocatalytic efficacy in comparison to the unmodified counterpart  $Zn_{0.5}Mn_{0.5}Fe_2O_4$ ,  $Ag/AgVO_3$ , and  $AgVO_3$ . The results of the recycling test demonstrated that the improved photocatalyst possesses superior photostability and reusability features.

The experiment with radical trapping provided evidence that 'OH and h<sup>+</sup> play a crucial role in the degradation process of Rh B. Therefore, the results presented above demonstrated that the Zn<sub>0.5</sub>Mn<sub>0.5</sub>Fe<sub>2</sub>O<sub>4</sub>/Ag/AgVO<sub>3</sub> nanocomposite photocatalyst, in its initial condition, exhibits promising promise as an efficient agent for the breakdown of organic contaminants commonly present in wastewater. Microrods of Ag/AgVO3 were embedded in a matrix of metal ferrite microspheres, which were distributed evenly throughout. The removal efficiency of degradation of the Zn<sub>0.5</sub>Mn<sub>0.5</sub>Fe<sub>2</sub>O<sub>4</sub>/Ag/AgVO<sub>3</sub> composite was significantly higher than that of pure Zn<sub>0.5</sub>Mn<sub>0.5</sub>Fe<sub>2</sub>O<sub>4</sub> and Ag/AgVO<sub>3</sub>. Degradation efficiency for Zn<sub>0.5</sub>Mn<sub>0.5</sub>Fe<sub>2</sub>O<sub>4</sub>/Ag/AgVO<sub>3</sub> composite is particularly high at 99.99% in just 180 min. The improved photocatalytic activity may be a result of efficient separations, charge transportations, and the absorption of visible light. Light absorption by the Ag/AgVO3 microrods was significantly increased in intensity and dramatically expanded in scope. Moreover, the supported nanocomposite was increased in intensity too. The characteristics of the nanocomposite were discussed deeply such as XRD, PL, DRS, VSM, FE-SEM, TEM, BET, and others.

The XRD peak locations of the produced Ag-AgVO<sub>3</sub> may be demonstrated to be nearly indistinguishable from those of the Zn<sub>0.5</sub>Mn<sub>0.5</sub>Fe<sub>2</sub>O<sub>4</sub>/Ag/AgVO<sub>3</sub> combination. When compared to other materials in its category, nanocomposite magnetization of 0.25 emu/g stands out as significantly lower. The supported hybrid could have a size ranging from 45.42 to 20.33 nm. Surface nanoparticles of zinc and manganese were present in the nanocomposite. The results of the EDS analysis expressed the chemical composition contributed to the synthesis of supported nanocomposite. With a lower bandgap energy, the supported Zn<sub>0.5</sub>Mn<sub>0.5</sub>Fe<sub>2</sub>O<sub>4</sub>/ Ag/AgVO<sub>3</sub> generates more electron/hole (e<sup>-</sup>/h<sup>+</sup>) pairs than the others. The specific surface area can contribute to the photocatalytic degradation. The results show that the AgVO<sub>3</sub> Nano rods successfully deposited Zn<sub>0.5</sub>Mn<sub>0.5</sub>Fe<sub>2</sub>O<sub>4</sub> on their surfaces. The results shown that after 180 min of exposure to VL, the photocatalyst was used to achieve a 70, 16.6, or 4.3% reduction

in TOC. Moreover, a reduction in the value of COD was shown after 240 min, leading to a 90% reduction. Thus, the characteristics of the supported nanocomposite show excellent results, enhancing the degradation performance of organic pollutants.

Furthermore, the incorporation of modified Ag nanoparticles leads to a substantial enhancement in the absorption of visible light by the samples. This enhancement is achieved by the induction of localized surface plasmon resonance (SPR), which arises from the collective oscillation of the surface electrons. In the photocatalytic process, the primary active species responsible for interacting with pollutants were the active holes (h $^+$ ). In addition, the composite photocatalyst of  $Zn_{0.5}Mn_{0.5}Fe_2O_4/Ag/AgVO_3$  showed remarkable durability. The (TOC) and (COD) were showed a reduction of 80-90% in removal efficiency. Reusing and stability were examined too for the supported nanocomposite and the optimum conditions were determined for the supported nanocomposite.

Funding information: Authors state no funding involved.

Author contributions: All authors have accepted responsibility for the entire content of this manuscript and consented to its submission to the journal, reviewed all the results and approved the final version of the manuscript. NAJ confirmed the study conception and design, data collection, analysis and interpretation of results, manuscript preparation. SEE and SHA conceived of the presented idea, developed the theory and performed the computations, verified the analytical methods. NAJ, SEE and SHA carried out the experiment. NAJ wrote the manuscript with support from co-authors. All authors discussed the results and contributed to the final manuscript.

Conflict of interest: Authors state no conflict of interest.

**Data availability statement:** Most datasets generated and analyzed in this study are in this submitted manuscript. The other datasets are available on reasonable request from the corresponding author with the attached information.

#### References

- [1] Jasim N, Ebrahim SE, Ammar S. Fabrication of ZnxMn1-xFe2O4 metal ferrites for boosted photocatalytic degradation of Rhodamine-B dye. Results Opt. 2023;13:100508. doi: 10.1016/j.rio. 2023.100508.
- [2] Su C, Zhang D, Pu X, He Z, Hu X, Li L, et al. Magnetically separable NiFe2O4/Ag3VO4/Ag2VO2PO4 direct Z-scheme heterostructure with enhanced visible-light photoactivity. J Chem Technol Biotechnol. 2021;96:2976–85. doi: 10.1002/jctb.6855.

- [3] Jasim N, Ebrahim SE, Ammar S. Photocatalytic degradation of Rhodamine B using CoxZn1-xFe2O4 nanocomposite under visible light irradiation: Synthesis, characterization and its application. Alex Eng J. 2023;82:557–76. doi: 10.1016/j.aej.2023.09.081.
- [4] Jasim N, Ammar S, Ebrahim SE. Assembling ZnMnFe2O4@Ag-AgVO3 nanostructure heterojunctions for photocatalytically degrading RhB and Pseudomonas aeruginosa bacteria under visible irradiation. J Photochem Photobiol A: Chem. 2023;449:115380. doi: 10.1016/j.jphotochem.2023.115380.
- [5] Abazari R, Mahjoub AR. Potential applications of magnetic β-AgVO3/ZnFe2O4 nanocomposites in dyes, photocatalytic degradation, and catalytic thermal decomposition of ammonium perchlorate. Ind Eng Chem Res. 2017;56(3):623–34.
- [6] Liu B, Lilong M, Han X, Zhang J, Shi H. Highly efficient visible-light-driven photocatalytic activity of g-C<sub>3</sub>N<sub>4</sub>@Ag/AgVO<sub>3</sub> composites for dye degradation and bacterial inactivation. J Photochem Photobiol A: Chem. 2019. doi: 10.1016/j.jphotochem.2019.111866.
- [7] Jasim N, Ebrahim SE, Ammar S. A comprehensive review on photocatalytic degradation of organic pollutants and microbial inactivation using Ag/AgVO3 with metal ferrites based on magnetic nanocomposites. Cogent Eng. 2023;10(1):2228069. doi: 10.1080/ 23311916.2023.2228069.
- [8] Nguyen LT, Vo DV, Nguyen LT, Duong AT, Nguyen HQ, Chu NM, et al. Synthesis, characterization, and application of ZnFe<sub>2</sub>O<sub>4</sub>@ZnO nanoparticles for photocatalytic degradation of Rhodamine B under visible-light illumination. Environ Technol Innov. 2021;25:102–30. doi: 10.1016/j.eti.2021.102130.
- [9] Yao X, He JH. On fabrication of nanoscale non-smooth fibers with high geometric potential and nanoparticle's non-linear vibration. Therm Sci. 2020;24(4):2491–7.
- [10] Lu Y, Hou X, Cheng K, Feng W. Photocatalytic properties of TiO2 induced by ZnFe2O4 nanoparticles under visible light irradiation. J Adv Oxid Technol. 2015;18(2):331–8. doi: 10.1515/jaots-2015-0220.
- [11] Tian D, Li X-X, He J-H. Geometrical potential and nanofiber membrane's highly selective adsorption property. Adsorpt Sci Technol. 2019;37(5–6):367–88. doi: 10.1177/0263617418813826.
- [12] Kharisov BI, Dias HR, Kharissova OV. Mini-review: Ferrite nanoparticles in the catalysis. Arab J Chem. 2019;12(7):1234–46.
- [13] Balasubramanian R, Abishek A, Gobinath S, Jaivignesh K. Alternative fuel: Hydrogen and its thermodynamic behaviour. J Hum Earth Future. 2022;3(2):195–203. doi: 10.28991/HEF-2022-03-02-05.
- [14] Jabbar ZH, Okab AA, Graimed BH, Issa MA, Ammar SH. Photocatalytic destruction of Congo red dye in wastewater using a novel Ag<sub>2</sub>WO<sub>4</sub>/Bi<sub>2</sub>S<sub>3</sub> nanocomposite decorated g-C<sub>3</sub>N<sub>4</sub> nanosheet as ternary S-scheme heterojunction: Improving the charge transfer efficiency. Diam Relat Mater. 2023;133:109711.
- [15] Jabbar TA, Ammar SH. Core/shell phosphomolybdic acid-supported magnetic silica nanocomposite (Ni@SiO2-PMo): Synthesis, characterization and its application as a recyclable antibacterial agent. Colloid Interface Sci Commun. Nov 2019;33:100214.
- [16] Yuan P, Qu X, Huang S, Xue X, Yuan X, Wang C, et al. Design of coreshelled g-C3N4@ZIF-8 photocatalyst with enhanced tetracycline adsorption for boosting photocatalytic degradation. Chem Eng J. 2021;416:129148.
- [17] Chen W, Xu N, Xu L, Wang L, Li Z, Ma W, et al. Multifunctional magnetoplasmonic nanoparticle assemblies for cancer therapy and diagnostics (theranostics). Macromol Rapid Comm. 2010;31:228–36.
- [18] Ajormal F, Moradnia F, Taghavi Fardood S, Ramazani A. Zinc ferrite nanoparticles in photo-degradation of dye: Mini-review. J Chem Rev. 2020;2(2):90–102. doi: 10.33945/SAMI/JCR.2020.2.2.

- [19] Shakil M, Inayat U, Arshad MI, Nabi G, Khalid NR, Tariq NH, et al. Influence of zinc and cadmium co-doping on optical and magnetic properties of cobalt ferrites. Ceram Int. 2020;46(6):7767–73. 0272-8842 doi: 10.1016/j.ceramint.2019.11.280.
- [20] Jamil A. Cu<sup>2+</sup> doped nickel spinel ferrites (CuxNi1–xFe2O4) nanoparticles loaded on CNTs for degradation of crystal violet dye and antibacterial activity studies. J Taibah Univ Sci. 2021;15(1):814–25. doi: 10.1080/16583655.2021.2005911.
- [21] Al-Alawy AF, Al-Abodi EE, Kadhim RM. Synthesis and characterization of magnetic iron oxide nanoparticles by co-precipitation method at different conditions. J Eng. 2018;24(10):60–72. doi: 10. 31026/j.eng.2018.10.05.
- [22] Moradi A, Elahinia M, Vasseghian A, Dragoi Y, Omidi EN, Khaneghah F. A review on pollutants removal by Sono-photo-Fenton processes. J Env Chem Eng. 2020;8(5):104330.
- [23] Alkurdy F, Ebrahim S. Comparison between commercial and synthesized Fe<sub>3</sub>O<sub>4</sub> nanoparticles for removal of heavy metal contaminants in wastewater. Assoc Arab Univ J Eng Sci. 2020;27(1):30–43. doi: 10.33261/jaaru.2019.27.1.004.
- [24] Bayantong AR, Shih YJ, Ong DC, Abarca RR, Dong CD, de Luna MD. Adsorptive removal of dye in wastewater by metal ferriteenabled graphene oxide nanocomposites. Chemosphere. 2021;274:129–518. doi: 10.1016/j.chemosphere.2020.129518. https://www.sciencedirect.com/science/article/pii/ S0045653520337164.
- [25] Singh A, Dutta DP, Ballal A, Tyagi AK, Fulekar MH. Visible light driven photocatalysis and antibacterial activity of AgVO<sub>3</sub> and Ag/ AgVO<sub>3</sub> nanowires. Mater Res Bull. 2014;51:447–54. doi: 10.1016/j. materresbull.2014.01.001.
- [26] Gao L, Li Z, Liu J. Facile synthesis of  $Ag_3VO_4/\beta$ -Ag $VO_3$  nanowires with efficient visible-light photocatalytic activity. RSC Adv. 2017;7:27515–2752144. doi: 10.1039/C7RA03955G.
- [27] Nurhasanah I. )Photodegradation of Rhodamine B by using  ${\sf ZnFe_2O_4}$  nanoparticles synthesized through precipitation method. IOP Conference Series: Materials Science and Engineering. Vol. 202, 2017.
- [28] Ahmed HA, Ebrahim SE. Removal of methylene blue and congo red dyes by pre-treated fungus biomass – equilibrium and kinetic studies. | Adv Res Fluid Mech Therm Sci. 2020;66(2):84–100.
- [29] Faraji A, Mehrdadi N, Mahmoodi NM, Baghdadi M, Pardakhti A. Enhanced photocatalytic activity by synergic action of ZIF-8 and NiFe<sub>2</sub>O<sub>4</sub> under visible light irradiation. J Mol Structure. 2021;1223:129028. doi: 10.1016/j.molstruc.2020.129028.
- [30] Kefeni KK, Mamba BB. Photocatalytic application of spinel ferrite nanoparticles and nanocomposites in wastewater treatment: Review. Sustain Mater Technol. 2020;23:e00140. doi: 10.1016/j. susmat.2019.e00140.
- [31] Dumitru V, Negrea S, Pacurariu C, Surdu A, Ianculescu A, Pop A, et al. CuBi<sub>2</sub>O<sub>4</sub> Synthesis, characterization, and application in sensitive amperometric/voltametric detection of amoxicillin in aqueous solutions. Nanomaterials. 2021;11:740.
- [32] Kumar M. Performance analysis of photolytic, photocatalytic, and adsorption systems in the degradation of metronidazole on the perspective of removal rate and energy consumption. Water Air Soil Pollut. 2017;228(9):228–339. https://link.gale.com/apps/doc/A501396690/AONE?u=anon~82bcb450&sid=googleScholar&xid=febe8/ah
- [33] Duong HDT, Nguyen DT, Kim K-S. Effects of process variables on properties of CoFe<sub>2</sub>O<sub>4</sub> nanoparticles prepared by solvothermal process. Nanomaterials. 2021;11:3056.

- [34] Nguyen LTT, Nguyen HTT, Le TH, Nguyen LTH, Nguyen HQ, Pham TTH, et al. Enhanced photocatalytic activity of spherical Nd<sup>3+</sup> substituted ZnFe<sub>2</sub>O<sub>4</sub> nanoparticles. Materials. 2021;14(8):2054. doi: 10.3390/ma14082054.
- [35] Aksoy M, Yanalak G, Aslan E, Patir IH, Metin Ö. Visible light-driven hydrogen evolution by using mesoporous carbon nitride-metal ferrite (MFe2O4/mpg-CN; M: Mn, Fe, Co and Ni) nanocomposites as catalysts. Int J Hydrog Energy. 2020;45:16509–18.
- [36] Ali N, Zada A, Zahid M, Ismail A, Rafiq M, Riaz A, et al. Enhanced photodegradation of methylene blue with alkaline and transitionmetal ferrite nanophotocatalysts under direct sun light irradiation. I Chin Chem Soc. 2018;66(4):1–7.
- [37] Casbeer E, Sharma VK, Li XZ. Synthesis and photocatalytic activity of ferrites under visible light: A review. Sep Purif Technol. 2012;87:1–14.
- [38] Chen D, Li B, Pu Q, Chen X, Wen G, Li Z. Preparation of  $Ag-AgVO_3/g-C_3N_4$  composite photo-catalyst and degradation characteristics of antibiotics. J Hazard Mater. 2019;5(373):303–12. doi: 10.1016/j. jhazmat.2019.03.090.
- [39] Mmelesi OK, Masunga N, Kuvarega A, Nkambule TT, Mamba BB, Kefeni KK. Cobalt ferrite nanoparticles and nanocomposites: Photocatalytic, antimicrobial activity and toxicity in water treatment. Mater Sci Semicond Process. 2021;123:105–523. doi: 10.1016/ j.mssp.2020.105523.
- [40] Ebrahim Shahlaa E. Comparison between dead anaerobic biomass and synthesized Fe<sub>3</sub>O<sub>4</sub> nanoparticles for the removal of Pb(II), Ni(II) and Cd(II). Desalin Water Treat. 2020;173:351–66.
- [41] Oluwole AO, Olatunji OS. Photocatalytic degradation of tetracycline in aqueous systems under visible light irridiation using needle-like SnO<sub>2</sub> nanoparticles anchored on exfoliated g-C<sub>3</sub>N<sub>4</sub>. Env Sci Eur. 2022;34:5. doi: 10.1186/s12302-021-00588-7.
- [42] Ju P, Wang Y, Sun Y, Zhang D. In-situ green topotactic synthesis of a novel Z-scheme  $Ag@AgVO_3/BiVO_4$  heterostructure with highly enhanced visible-light photocatalytic activity. J Colloid Interface Sci. 2020;579:431–47. doi: 10.1016/j.jcis.2020.06.094.
- [43] Rafaie HA, Ramli NIT, Khusaimi Z, Mohd Sarjidan MA, Dulyaseree P, Hir ZAM. Ag2CO3-based photocatalyst with enhanced photocatalytic activity for endocrine-disrupting chemicals degradation: A review. Catalysts. 2023;13:540. doi: 10.3390/catal13030540.
- [44] Qin C, Lei S, Tang X, Zhong J, Li J, He J. Preparation of novel Ag/ AgVO<sub>3</sub>/BiVO<sub>4</sub> heterojunctions with significantly enhanced visible light-driven photocatalytic performance originated from Z-scheme separation of photogenerated charge pairs. Inorg Chem Commun. 2020;116:107904. doi: 10.1016/j.inoche.2020.107-904.
- [45] Rotjanasuworapong K, Lerdwijitjarud W, Sirivat A. Synthesis and characterization of Fe<sub>0.8</sub>Mn<sub>0.2</sub>Fe<sub>2</sub>O<sub>4</sub> ferrite nanoparticle with high saturation magnetization via the surfactant assisted coprecipitation. Nanomaterials. 2021;11(4):876. doi: 10.3390/ nano11040876.
- [46] Shakil M, Inayat U, Tanveer M, Nabi G, Gillani SS, Rafique M, et al. NiO and Ag–Cd co-doped NiO nanoparticles: study of photocatalytic degradation of rhodamine B dye for wastewater treatment. Int J Env Sci Technol. 2022;20(4):2021–36. doi: 10.1007/s13762-022-04101-2.
- [47] Jabbar ZH, Ebrahim SE. Synthesis, characterization, and photocatalytic degradation activity of core/shell magnetic nanocomposites (Fe<sub>3</sub>O<sub>4</sub>@SiO<sub>2</sub>@Ag<sub>2</sub>WO<sub>4</sub>@Ag<sub>2</sub>S) under visible light irradiation. Optical Mater. 2021;122. doi: 10.1016/j.optmat.2021.111818.
- [48] Singh P, Shandilya P, Raizada P, Sudhaik A, Rahmani-Sani A, Hosseini-Bandegharaei A. Review on various strategies for

- enhancing photocatalytic activity of graphene based nanocomposites for water purification. Arab J Chem. 2020;13:3498–520.
- [49] Swady EA, Jawad MK. Study FTIR and AC conductivity of nanocomposite electrolytes. IJP. 2021;19(51):15–22. https://ijp. uobaghdad.edu.iq/index.php/physics/article/view/689.
- [50] Thakre KG, Barai DP, Bhanvase BA. A review of graphene-TiO<sub>2</sub> and graphene-ZnO nanocomposite photocatalysts for wastewater treatment. Water Env Res. 2021 Nov;93(11):2414–60. doi: 10.1002/ wer.1623. Epub 2021 Sep 22. PMID: 34378264.
- [51] Jeseentharani V, George M, Jeyaraj B, Dayalan A, Nagaraja KS. Synthesis of metal ferrite (MFe<sub>2</sub>O<sub>4</sub>, M = Co, Cu, Mg, Ni, Zn) nanoparticles as humidity sensor materials. J Exp Nanosci. 2013;8(3):358–70. doi: 10.1080/17458080.2012.690893.
- [52] Manikandan V, Mahadik MA, Hwang IS, Chae WS, Ryu J, Jang JS. Visible-light-active CuOx-loaded Mo-BiVO4 photocatalyst for inactivation of harmful bacteria (Escherichia coli and Staphylococcus aureus) and degradation of orange II dye. ACS Omega. 2021;6(37):23901–12. doi: 10.1021/acsomega.1c02879.
- [53] Dutta S, Akhter M, Ahmed J, Amin MK, Palash Dhar K. Synthesis and catalytic activity of spinel ferrites: A brief review. Biointerface Res Appl Chem. 2021:12(6):4399–416.
- [54] Farhan AM, Zaghair AM, Abdullah HI. Adsorption study of Rhodamine – B dye on plant (Citrus Leaves). Baghdad Sci J. 2022;19(4):0838.
- [55] Zhao W, Li J, bo Wei Z, Wang S, He H, Sun C, et al. Fabrication of a ternary plasmonic photocatalyst of Ag/AgVO3/RGO and its excellent visible-light photocatalytic activity. Appl Catal B, Environ. 2015;179:9–20 doi: 10.1016/j.apcatb.2015.05.002.
- [56] Jabbar ZH, Ebrahim SE. Recent advances in nano-semiconductors photocatalysis for degrading organic contaminants and microbial disinfection in wastewater: A comprehensive review. Environ Nanotechnol Monit Manag. 2022;17:0925–3467. doi: 10.1016/j. enmm.2022.100666.
- [57] Mohamed S, Kareem N. Optical properties for prepared polyvinyl alcohol/polyaniline/ZnO nanocomposites. IJP. 2018;16(36):181–9, https://ijp.uobaghdad.edu.iq/index.php/physics/article/view/42.
- [58] Xian G, Kong S, Li Q, Zhang G, Zhou N, Du H, et al. Synthesis of spinel ferrite MFe<sub>2</sub>O<sub>4</sub> (M = Co, Cu, Mn, and Zn) for persulfate activation to remove aqueous organics: Effects of M-site metal and synthetic method. Front Chem. 2020;8:177. doi: 10.3389/fchem.2020.00177. PMID: 32266209: PMCID: PMC7105867.
- [59] Mapossa AB, Mhike W, Adalima JL, Tichapondwa S. Removal of organic dyes from water and wastewater using magnetic ferritebased titanium oxide and zinc oxide nanocomposites: A review. Catalysts. 2021;11:1543. doi: 10.3390/catal11121543.
- [60] Fu Y, Wang X. Magnetically separable  $ZnFe_2O_4$ –graphene catalyst and its high photocatalytic performance under visible light irradiation. Ind & Eng Chem Res. 2011;50(12):7210–8. doi: 10.1021/ie200162a.
- [61] Dong H, Zeng G, Tang L, Fan C, Zhang C, He X, et al. An overview on limitations of TiO₂-based particles for photocatalytic degradation of organic pollutants and the corresponding countermeasures. Water Res. 2015;79:128–46. doi: 10.1016/j.watres.2015.04.038.
- [62] Jing L, Xu Y, Huang S, Xie M, He M, Xu H, et al. Novel magnetic CoFe<sub>2</sub>O<sub>4</sub>/Ag/Ag<sub>3</sub>VO<sub>4</sub> composites: Highly efficient visible light photocatalytic and antibacterial activity. Appl Catal B-environmental. 2016;199:11–22.
- [63] Kosslick H, Wang YY, Ibad MF, Guo XY, Lütgens M, Lochbrunner S, et al. High-performance room-light-driven β-AgVO<sub>3</sub>/mpg-C<sub>3</sub>N<sub>4</sub>

- core/shell photocatalyst prepared by mechanochemical method. Adv Chem Eng Sci. 2021;11:290-315. doi: 10.4236/aces.2021.114018.
- [64] Chen Y, Liang Y, Zhao M, Wang Y, Zhang L, Jiang Y, et al. In-situ ion exchange synthesis of Ag2S/AgVO3 graphene aerogels for enhancing photocatalytic antifouling efficiency. Ind & Eng Chem Res. 2019;58(8):3538-48. doi: 10.1021/acs.iecr.8b05962.
- [65] Tanveer M, Nisa I, Nabi G, Shakil M, Khalid S, Qadeer MA. Enhanced structural, optical, and photocatalytic activity of novel Cd-Zn codoped Mg<sub>0.25</sub> Fe<sub>1.75</sub>O<sub>4</sub> for degradation of Rh B dye under visible light irradiation. Ceram Int. 2022;48(11):15451-61. doi: 10.1016/j. ceramint.2022.02.079.
- [66] Yao Y, Cai Y, Lu F, Qin J, Wei F, Xu C, et al. Magnetic ZnFe<sub>2</sub>O<sub>4</sub>-C<sub>3</sub>N<sub>4</sub> hybrid for photocatalytic degradation of aqueous organic pollutants by visible light. Ind & Eng Chem Res. 2014;53(44):17294-302. doi: 10.1021/ie503437z.
- [67] Gupta NK, Ghaffari Y, Kim S, Bae J, Kim KS, Saifuddin M. Photocatalytic degradation of organic pollutants over MFe<sub>2</sub>O<sub>4</sub> (M = Co, Ni, Cu, Zn) nanoparticles at neutral pH. Sci Rep. 2020;10:4942. doi: 10.1038/s41598-020-61930-2.
- [68] Kotal M, Sharma A, Jakhar S, Mishra V, Roy S, Sahoo SC, et al. Graphene-templated cobalt nanoparticle embedded nitrogendoped carbon nanotubes for efficient visible-light photocatalysis. Cryst Growth Des. 2020;20(7):4627-39. doi: 10.1021/acs.cgd. 0c00430.
- [69] Khadayeir AA, Wannas AH, Yousif FH. Effect of applying cold plasma on structural, antibacterial and self-cleaning properties of α-Fe<sub>2</sub>O<sub>3</sub> (HEMATITE) thin film. Emerg Sci J. 2022;6(1):2610-9182.
- [70] Aparna ML, Grace AN, Sathyanarayanan P, Sahu NK. A comparative study on the supercapacitive behaviour of solvothermally prepared metal ferrite (MFe2O4, M = Fe, Co, Ni, Mn, Cu, Zn) nanoassemblies. J Alloy Compd. 2018;745:385-95.
- [71] Azzaz AA, Jellali S, Hamed NBH, El Jery A, Khezami L, Assadi AA, et al. Photocatalytic treatment of wastewater containing simultaneous organic and inorganic pollution: competition and operating para-

- meters effects. Catalysts. 2021;11(7):855. doi: 10.3390/ catal11070855.
- [72] Anchieta CG, Cancelier A, Mazutti MA, Jahn SL, Kuhn RC, Gündel A, et al. Effects of solvent diols on the synthesis of ZnFe<sub>2</sub>O<sub>4</sub> particles and their use as heterogeneous photo-Fenton catalysts. Mater (Basel). 2014 Sep;7(9):6281-90. doi: 10.3390/ma7096281, PMID: 28788191; PMCID: PMC5456135.
- [73] Zhao L, Yang H, Yu L, Sun W, Cui Y, Yan Y, et al. Structure and magnetic properties of Ni0.7Mn0.3Fe2O4 nanoparticles doped with La2O3. Phys Status Solidi (a). 2004;201:3121-8.
- Zhao W, Li J, Wei Z, Wang S, He H, Sun C, et al. Fabrication of a ternary plasmonic photocatalyst of Ag/AgVO<sub>3</sub>/RGO and its excellent visible-light photocatalytic activity. Appl Catal B-environmental. 2015:179:9-20.
- [75] Zuliani A, Cova CM. Green synthesis of heterogeneous visible-lightactive photocatalysts: Recent advances. Photochem. 2021;1(2):147-66. doi: 10.3390/photochem1020009.
- [76] Ebrahime SE, Alsaade SH. Competitive adsorption of Cd(II) and Zn(II) in single and binary systems from aqueous solutions onto cork stopper particles. J Eng Sci Soc Eng Coll. 2019:26(1):17-27.
- [77] Fatima N, Tanveer M, Nawaz T, Tahir MB, Sagir M, Rafique M, et al. Synthesis of ZnO/Ag/phosphorene for photocatalytic reduction of hexavalent chromium (Cr-VI). Appl Nanosci. 2022;12:2379-87. doi: 10.1007/s13204-022-02509-3.
- Jabbar ZH, Ammar SH, Ebrahim SE. Enhanced visible-light photocatalytic bacterial inhibition using recyclable magnetic heterogeneous nanocomposites ( $Fe_3O_4@SiO_2@Ag_2WO_4@Ag_2S$ ) in core/shell structure. Environ Nanotechnol Monit Manag. 2021;16:1369-8001. doi: 10.1016/j.enmm.100601.
- [79] Kokkinos P, Mantzavinos D, Venieri D. Current trends in the application of nanomaterials for the removal of emerging micropollutants and pathogens from water. Molecules. 2016;25(9):1-32. doi: 10.3390/molecules25092016.